Measurement of the charge asymmetry of electrons from the decays of W bosons produced in p̄p collisions at √ s = 1.96 TeV

Author(s):
CDF Collaboration; Aaltonen, Timo A.; Casal, Bruno; Marchese, Luigi; Wallny, Rainer ⓘD; et al.

Measurement of the charge asymmetry of electrons from the decays of W bosons produced in $p\bar{p}$ collisions at $\sqrt{s} = 1.96$ TeV

T. Aaltonen *et al.*[*]

(CDF Collaboration)

At the Fermilab Tevatron proton-antiproton ($p\bar{p}$) collider, high-mass electron-neutrino ($e\nu$) pairs are produced predominantly in the process $p\bar{p} \to W(\to e\nu) + X$. The asymmetry of the electron and positron yield as a function of their pseudorapidity constrain the slope of the ratio of the u- to d-quark parton distributions versus the fraction of the proton momentum carried by the quarks. This paper reports on the measurement of the electron-charge asymmetry using the full data set recorded by the Collider Detector at Fermilab in 2001–2011 and corresponding to 9.1 fb^{-1} of integrated luminosity. The measurement significantly improves the precision of the Tevatron constraints on the parton-distribution functions of the proton. Numerical tables of the measurement are provided.

I. INTRODUCTION

At the Fermilab Tevatron proton-antiproton ($p\bar{p}$) collider, massive lepton pairs consisting of charged leptons (ℓ) and their partner neutrinos (ν) are produced in $p\bar{p}$ collisions at the center-of-momentum energy ($\sqrt{s}$) 1.96 TeV [1]. In the standard model, the $\ell\nu$ pair is produced through an intermediate W boson whose production occurs primarily through the quark-antiquark annihilation process,

$$q + \bar{q}' \to W \to \ell\nu,$$

where the q and $\bar{q}'$ denote the incoming quark and antiquark, respectively, from the colliding hadrons. In leading-order quantum chromodynamics (QCD) calculations, 90% of W^+ bosons are produced via $u + \bar{d}$ collisions and a similar fraction of W^- bosons via $d + \bar{u}$ collisions.

The production rates of W^+ and W^- bosons exhibit differences as functions of their kinematic properties over their kinematic range of production. The momentum distributions of the u ($\bar{u}$) and d ($\bar{d}$) quarks from the incoming proton (antiproton) differ, affecting the W^+ and W^- differential-production rates. Momentum distributions of quarks and gluons are determined by the parton-

distribution functions (PDFs) of the proton, which must be experimentally derived. Measurements of production-rate differences can be used to constrain the PDFs. A highly constraining measurement is the charged-lepton yield asymmetry as a function of pseudorapidity

$$A_\ell = \frac{d\sigma_\ell^+/d\eta - d\sigma_\ell^-/d\eta}{d\sigma_\ell^+/d\eta + d\sigma_\ell^-/d\eta}, \tag{1}$$

where $d\sigma_\ell^\pm/d\eta$ denotes the differential cross section with respect to the pseudorapidity η of charged leptons $\ell^\pm$ from the production of $W^\pm$ bosons and their subsequent decay via $W \to \ell\nu$. The pseudorapidity is $-\ln\tan(\theta/2)$, where θ is the polar angle of the lepton relative to the proton direction. Effects from the interference between the axial and vector currents of the electroweak interaction, and from the initial-state interactions of the colliding partons alter the boson asymmetries. While the leptonic asymmetry A_ℓ can be measured well, its interpretation in terms of the underlying PDFs must include these effects. The Tevatron measurement of A_ℓ constrains the slope of the ratio of the d- to u-quark distribution functions as a function of the Bjorken scaling parameter, the fraction x of the proton momentum taken by the colliding quark [2].

The leptonic asymmetry A_ℓ has been measured at the Tevatron collider with $p\bar{p}$ collisions and at the Large Hadron Collider (LHC) with pp collisions. Tevatron measurements have been reported at $\sqrt{s} = 1.8$ TeV by CDF [3], and at $\sqrt{s} = 1.96$ TeV by CDF [4] and D0 [5–8]. The boson-level asymmetry has also been inferred at $\sqrt{s} = 1.96$ TeV by CDF [9] and D0 [10] using a neutrino-weighting technique [11]. The LHC measurements at

---

[*]Full author list given at the end of the article.

$\sqrt{s} = 7$ (8) TeV have been reported by ATLAS [12,13], CMS [14–16] (CMS [17]), and LHCb [18] (LHCb [19,20]). Measurements from colliders of different types and energies provide important constraints for global fits of PDFs because the compositions of input parton fluxes that produce W bosons differ, and because the increased precision attainable significantly improves the accuracy of the fitted PDFs. At the LHC, W bosons are mostly produced through quark-antiquark collisions as they are at the Tevatron. However, at the Tevatron, the collisions are primarily between valence quarks while at the LHC, collisions are primarily between valence and sea quarks.

In this paper, the final CDF measurement of the asymmetry A_ℓ in the $W \to e\nu$ channel[1] is presented, using a data sample corresponding to an integrated $p\bar{p}$ luminosity of 9.1 fb^{-1} collected at the Tevatron collider. This measurement supersedes the previous CDF measurements [4,9], that were based on subsamples at least nine times smaller.

Section II of the paper provides an overview of the formal definition of the asymmetries and of the existing theoretical calculations. Section III introduces the asymmetry measured in this paper. Section IV describes the experimental apparatus. Section V reports on the selection of data. Section VI describes the simulation of the reconstructed data. Section VII presents an overview of the corrections to the data and simulation, and Sec. VIII the details of those corrections. Section IX presents the measurement of the asymmetry, Sec. X the systematic uncertainties, and Sec. XI the results. Finally, Sec. XII presents a summary.

II. ASYMMETRY DISTRIBUTIONS

In the laboratory frame, the $p\bar{p}$-collision axis is the z axis, with the positive direction oriented along the direction of the proton. The transverse component of any vector quantity is defined relative to that axis. The rapidity, transverse momentum, and mass of a particle are denoted as y, $\vec{P}_{\rm T}$, and M, respectively. The energy and momentum of particles are denoted as E and $\vec{P}$, respectively. The rapidity is $y = \frac{1}{2}\ln[(E + P_z)/(E - P_z)]$, where P_z is the component of the momentum vector along the z axis. For massless particles, the rapidity reduces to the pseudorapidity η.

The cross section for the production of W bosons in hadronic collisions, differential in the rapidity, squared mass, and squared transverse momentum, is denoted by $d^3\sigma_W/dydP_{\rm T}^2dM^2$. The charge asymmetry at a given y value is defined as

$$A_W = \frac{d\sigma_W^+/dy - d\sigma_W^-/dy}{d\sigma_W^+/dy + d\sigma_W^-/dy}, \qquad (2)$$

---

[1]The $W \to \mu\nu$ channel is not considered due to the limited η coverage and complexity of the muon measurement.

where $d\sigma_W^\pm/dy$ denotes the cross section for $W^\pm$ production integrated over $P_{\rm T}^2$ and M^2.

Since the P_z component of the neutrino momentum cannot be measured on an event-by-event basis, the charge asymmetry of the lepton $A_\ell(\eta)$ is measured. The cross-section input to $A_\ell(\eta)$ is a combination of the W-boson cross section and the angular distribution of the $\ell\nu$ pair from the W-boson decay in the rest frame of the $\ell\nu$ pair,

$$\frac{d^5\sigma_{\ell\nu}}{dydP_{\rm T}^2dM^2d\cos\vartheta d\varphi} = \frac{3}{16\pi}\frac{d^3\sigma_W}{dydP_{\rm T}^2dM^2}\mathcal{N}(\vartheta, \varphi),$$

where the angular-distribution function $\mathcal{N}(\vartheta, \varphi)$ is the density of W decays as a function of the polar angle ϑ and azimuthal angle φ of the charged lepton, respectively, and the charge-specific labels for the W-boson cross section and angular-distribution function are implicit. The decay into the lepton pair exposes a set of helicity cross sections that characterize the density matrix of the W-boson polarization states that are produced.

In this analysis, the Collins-Soper (CS) rest frame of the $\ell\nu$ pair is used to quantify $\mathcal{N}(\vartheta, \varphi)$ [21]. This frame is reached from the laboratory frame via two Lorentz boosts, first along the laboratory z-axis into the frame where the z component of the $\ell\nu$-pair momentum vector is zero, followed by a boost along the transverse component of the $\ell\nu$-pair momentum vector into its rest frame. A view of the CS frame is shown in Fig. 1.

The angular-distribution function is expressed as

$$\mathcal{N}(\vartheta, \varphi) = (1 + \cos^2\vartheta) + A_0\frac{1}{2}(1 - 3\cos^2\vartheta)$$
$$+ A_1\sin 2\vartheta\cos\varphi + A_2\frac{1}{2}\sin^2\vartheta\cos 2\varphi$$
$$+ A_3\sin\vartheta\cos\varphi + A_4\cos\vartheta$$
$$+ A_5\sin^2\vartheta\sin 2\varphi + A_6\sin 2\vartheta\sin\varphi$$
$$+ A_7\sin\vartheta\sin\varphi, \qquad (3)$$

where A_{0-7} are coefficient functions that describe the nonangular parts of the helicity cross sections relative to the unpolarized cross section integrated over the polar angles [22]. In amplitudes at higher order than the tree level, initial-state interactions of the colliding partons impart transverse momentum to the boson, affecting the helicity cross sections. Consequently, A_{0-7} are functions of the W boson y, $P_{\rm T}$, and M. They vanish when the boson transverse momentum is zero, except for A_4 whose value is ± 2 for $W^\mp$ decays in QCD calculations at leading order (LO). In electroweak interactions, the interference between the vector and axial currents produces the $A_4\cos\vartheta$ term. The A_{5-7} coefficients appear at second order in the QCD strong-coupling constant, α_s, and are small in the CS frame.
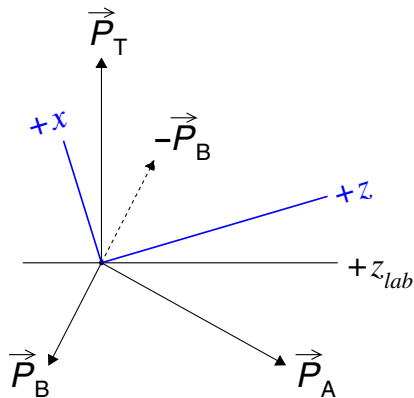
FIG. 1.   Representation of the CS-coordinate axes (x, z) along with the laboratory z axis (z_{lab}). The three axes are in the plane formed by the proton $(\vec{P}_A)$ and antiproton $(\vec{P}_B)$ momentum vectors in the $\ell\nu$-pair rest frame. The z axis is the angular bisector of $\vec{P}_A$ and $-\vec{P}_B$, the y axis is along the direction of $\vec{P}_B \times \vec{P}_A$, and the x axis is in the direction away from the transverse component of $\vec{P}_A + \vec{P}_B$. In the limit of vanishing P_T, the CS and laboratory axes become equivalent.

For the W-boson cross sections used in comparisons of measurements to theoretical predictions, next-to-leading-order (NLO) QCD calculations (of order α_s) and recent PDFs are used. The POWHEG-BOX[2] implementation of W-boson production [23] and decay to lepton pairs [24] provides the NLO QCD calculation. It is used as an unweighted partonic event generator. The NLO-production framework implements a Sudakov form factor that controls the infrared divergence at low-boson P_T [25], and an interface to parton-showering algorithms that avoids double counting. The PYTHIA 6.41 parton-showering algorithm is used to produce the hadron-level event [26]. The combined implementation has next-to-leading log resummation accuracy. Parton fluxes of the incoming proton and antiproton are provided by the recent NNPDF 3.0 set of NLO PDFs derived with the value of $\alpha_s = 0.118$ at the Z-pole mass [27]. The POWHEG-BOX calculation with the NNPDF 3.0 NLO PDFs is the default calculation.

In addition, the RESBOS NLO calculation [28] with CTEQ6.6 NLO PDFs [29] is used for the ancillary tuning of W-boson production within the POWHEG-BOX calculation. The RESBOS calculation combines an NLO fixed-order calculation at high boson P_T with the Collins-Soper-Sterman resummation formalism [30] at low boson P_T, which is an all-orders summation of large terms from gluon emission calculated to next-to-next-to-leading log accuracy. The intrinsic P_T parameters of PYTHIA 6.41 used for the default calculation are adjusted [3] so that the boson P_T

_____

[2]The POWHEG-BOX code is version V2 (svn 3319).

[3]The adjusted parameters and values are: MSTP(91) = 1, PARP(91) = 1.50 GeV/c, PARP(93) = 12 GeV/c, and PARP(64) = 0.4.
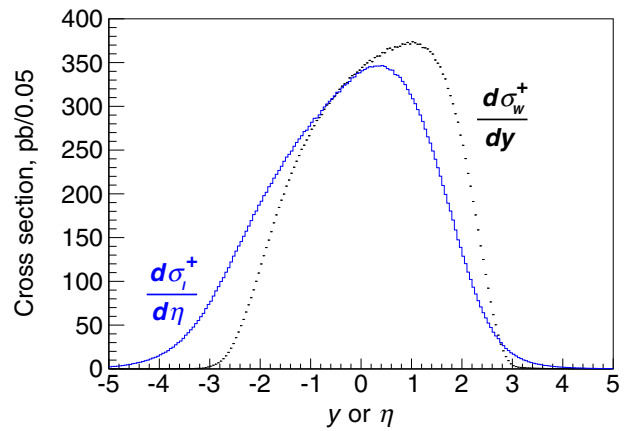

FIG. 2. $d\sigma_W^+/dy$ and $d\sigma_\ell^+/d\eta$ cross sections. The cross section for W^+-boson (W-decay charged-lepton) production in 1.96 TeV proton-antiproton collisions as a function of the rapidity (pseudorapidity). The cross sections are from the default calculation.

distribution of the region below 30 GeV/c is in good agreement with that from the RESBOS calculation. The RESBOS calculation of the γ^*/Z P_T distribution in $p\bar{p}$ collisions, which is kinematically similar to W-boson production, agrees with the CDF measurement based on an integrated luminosity corresponding to 2.1 fb^{-1} [31].

The current known values for the W-boson pole mass M_W and resonant width Γ_W, 80.385 GeV/c^2 and 2.085 GeV [32], respectively, are used in the POWHEG-BOX and RESBOS calculations. Both calculations employ resonant line shapes for the boson-mass distribution with mass-dependent widths. CDF has modified the POWHEG-BOX calculation to use the recent values of the Cabibbo-Kobayashi-Maskawa matrix [33,34] elements associated with the weak-interaction charged current [32].

Figure 2 illustrates the $d\sigma_W^+/dy$ and $d\sigma_\ell^+/d\eta$ cross sections from the POWHEG-BOX calculation. Since the geometry of the colliding p and $\bar{p}$ system is asymmetric under the reversal of charge and parity (CP), the $d\sigma_W^-/dy$ and $d\sigma_\ell^-/d\eta$ cross sections in a coordinate frame whose positive-z axis is oriented along the antiproton direction are identical to those of the positive-charge cross sections shown in Fig. 2, where the positive-z axis is oriented along the proton direction. In the laboratory frame of Fig. 2, $d\sigma_W^-(y)/dy = d\sigma_W^+(-y)/dy$ and $d\sigma_\ell^-(\eta)/d\eta = d\sigma_\ell^+(-\eta)/d\eta$. Figure 3 illustrates the boson-level charge asymmetry $A_W(y)$ and the lepton-level charge asymmetry $A_\ell(\eta)$ based on the POWHEG-BOX calculation.

III. MEASURED ASYMMETRIES

Measurements of the charge asymmetry A_ℓ within a reconstructed pseudorapidity interval (bin) can be formally expressed using the observed cross section $\Delta\sigma = N/(\mathcal{L}\epsilon A)$, where N is the number of observed signal events after background subtraction, $\mathcal{L}$ the integrated luminosity, ϵ the event reconstruction and selection efficiency, and A the
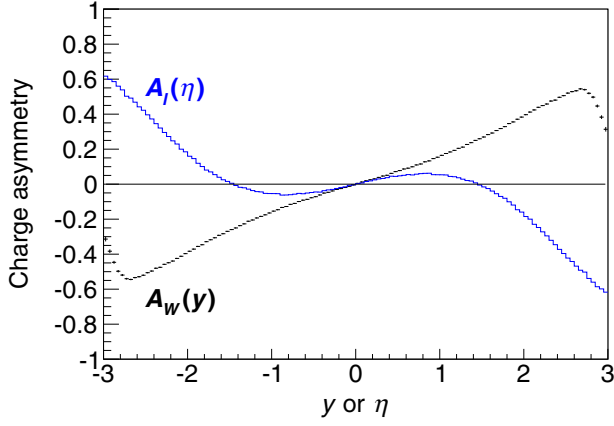
FIG. 3. $A_W(y)$ and $A_\ell(\eta)$ charge asymmetries. The charge-dependent W-boson (W-decay charged-lepton) yield asymmetries as functions of the rapidity (pseudorapidity). The asymmetry distributions are antisymmetric and from the default calculation.

acceptance of events within the kinematic and fiducial restrictions. When the expressions for the bin-level cross sections of the electrons and positrons are substituted into Eq. (1), the common integrated luminosity terms cancel out yielding

$$A_\ell = \frac{N^+/(\epsilon A)^+ - N^-/(\epsilon A)^-}{N^+/(\epsilon A)^+ + N^-/(\epsilon A)^-}, \qquad (4)$$

where $N^{+(-)}$ and $(\epsilon A)^{+(-)}$, respectively, represent the N and ϵA of positrons (electrons).

In this paper the asymmetry is measured using Eq. (4) over the positron- and electron-pseudorapidity range of -3 to 3 in uniform bins of width 0.2. As the positrons and electrons in each bin are within the same region of η, their reconstruction and selection efficiencies are expected to be similar except for those that are not charge symmetric. Relative to a cross-section measurement, the precision of a ratio of cross-section measurements such as the asymmetry is far less dependent on accurate measurements of all of the experimental efficiencies.

Details of the experimental apparatus, data set, simulation of the data, and corrections to the data used in the measurement follow in Secs. IV–VIII.

IV. EXPERIMENTAL APPARATUS

The CDF II apparatus is a general-purpose detector [35] at the Fermilab Tevatron, a $p\bar{p}$ collider with $\sqrt{s} = 1.96$ TeV. The Cartesian coordinates of the detector are denoted by x, y, and z. The coordinate system is right-handed with the positive-z axis directed along the proton direction and the positive-y axis directed vertically upwards. For particle trajectories, the polar angle θ is relative to the positive-z axis and the azimuthal angle ϕ is relative to the positive-x axis. Detector coordinates, denoted by $(\eta_{\text{det}}, \phi)$, are defined relative to the center of the detector ($z = 0$).

The curvature and momentum $\vec{P}$ of a charged particle are measured in the magnetic spectrometer, which consists of charged-particle position detectors (trackers) immersed in a magnetic field. The energy E of photons, electrons, and hadrons is measured by the calorimeters surrounding the magnetic spectrometer. The measured energy in the calorimeters (energy flow) transverse to the beam line is $E_T = E \sin\theta$.

The tracking detectors consist of an outer central tracker and an inner tracker. The central tracker is a 3.1 m long, open-cell drift chamber [36] that extends radially from 0.4 to 1.4 m. Between the Tevatron beam pipe and the central tracker is a 2 m long silicon-microstrip inner tracker [37]. The central drift-chamber tracker has 96 tracking layers, and the silicon tracker has seven or eight tracking layers depending on η_{det}. Both trackers are immersed in a 1.4 T axial magnetic field produced by a superconducting solenoid beyond the outer radius of the drift chamber. Combined, these two trackers provide efficient, high-resolution tracking and momentum measurement over $|\eta_{\text{det}}| < 1.3$.

Outside the solenoid is the central-barrel calorimeter that covers the region $|\eta_{\text{det}}| < 1.1$ [38,39]. The forward regions, $1.1 < |\eta_{\text{det}}| < 3.5$, are covered by disk-shaped end-plug calorimeters [40–42]. The electromagnetic (EM) and hadronic (HAD) sections of the calorimeters are scintillator-based sampling calorimeters, transversely segmented into projective towers that point back to the center of the detector. The EM-calorimeter energy resolutions measured in test beams with electrons are $\sigma/E = 13.5\%/\sqrt{E_T}$ for the central calorimeter and $\sigma/E = (16\%/\sqrt{E}) \oplus 1\%$ for the plug calorimeter, where the symbol $\oplus$ is a quadrature sum, and E_T and E are in units of GeV. Both the central- and plug-EM calorimeters have preshower and shower-maximum detectors for electromagnetic-shower identification and centroid measurements. The shower-maximum detectors within the central- and plug-EM calorimeters are strip detectors, and are denoted by CES and PES, respectively.

The combination of the PES detector and silicon tracker provides enhanced electron-tracking coverage to $|\eta_{\text{det}}| = 2.8$. A PES detector consists of eight 45° wedge-shaped subdetectors assembled into a disk. Subdetector wedges consist of "strips" made of 5×5 mm^2 scintillator bars organized into two parallel planes, denoted by u and v, that span the length of the fiducial region of the measurement. The u strips are parallel to one radial edge, and the v are parallel to the other.

The presence of neutrinos in $W \to \ell\nu$ events is inferred from the energy-flow measurements on all reconstructed particles in the event. The transverse momentum of the neutrino balances the vector sum of the transverse-energy flows. Thus, the negative of this vector sum, called the missing $\vec{E}_T$ and denoted by $\vec{\not{E}}_T$, is an estimator of the neutrino transverse momentum.

V. DATA SELECTION

The data set, collected over 2002–2011, is the full CDF Run II sample corresponding to an integrated $p\bar{p}$ luminosity of 9.1 fb^{-1}. After event selection, the sample consists of 5.8×10^6 events. Section V A reports on the online selection of events (triggers) for the charge-asymmetry measurement. Section V B describes the offline selection of electron candidates, and Sec. V C describes the selection of electron-neutrino pairs.

A. Online event selection

Event samples enriched in signal candidates are selected by means of two online triggers, CENTRAL-18 and PEM-20_MET-15. The CENTRAL-18 selection accepts events containing at least one electron candidate in the central calorimeter with $E_T > 18$ GeV. Candidates are required to have electromagnetic-shower clusters in the central calorimeters that are geometrically matched to tracks from the central tracker. The PEM-20_MET-15 selection accepts events with an electron candidate in the plug calorimeter with $E_T > 20$ GeV and with $\not{E}_T > 15$ GeV. Electron candidates in the plug region are not required to geometrically match a track extrapolation. Values of the E_T and $\not{E}_T$ quantities differ from the corresponding values of the offline quantities of Sec. V B due to more refined offline calibrations and calculation techniques.

B. Offline electron selection

The offline event reconstruction, which includes the application of standard electron identification and quality requirements, improves the purity of the sample [35]. Fiducial constraints are applied to ensure that the electron candidates are reconstructed in instrumented detector regions. Each electron candidate is required to be associated with a track whose origin along the beam line (z_{vtx}) is restricted to be within 97% of the luminous region, $|z_{vtx}| < 60$ cm.

Electron identification in the central region is optimized for electrons of $P_T > 10$ GeV/c [35]. It uses information from the central and silicon trackers, the longitudinal and lateral (tower) segmentation of the electromagnetic and hadronic calorimeter compartments, and the CES detector within the electromagnetic calorimeter. The highest quality of signal selection and background rejection is provided by the trackers in combination with the CES. An electron candidate must have an associated shower cluster within the electromagnetic-calorimeter towers and a CES signal compatible with the lateral profile of an electromagnetic shower. A candidate must also be associated with a track that extrapolates to the three-dimensional position of the CES shower centroid. The transverse momentum associated with the track must be consistent with the corresponding electron-shower E_T via an E/P selection

if $P_T < 50$ GeV/c [35]. For both the track matching in the CES and the E/P selection, allowances are included for bremsstrahlung energy loss in the tracking volume, where material thickness is on average 20% of a radiation length. The ratio of the measured shower energy in the hadronic calorimeter to that in the electromagnetic calorimeter, E_{HAD}/E_{EM}, must be consistent with that for electrons.

Electron identification in the plug calorimeter also uses information from the tracker, from the longitudinal and lateral (tower) segmentation of the electromagnetic and hadronic calorimeter compartments, and from the PES detector within the electromagnetic calorimeter. As the plug-calorimeter geometry differs from the central geometry, the details of the selection requirements differ.

The plug calorimeters, with sampling planes perpendicular to the beam line, have much smaller projective towers than the central calorimeter towers and vary in size as a function of $|\eta_{det}|$ [40]. The preshower detector is the first layer of the electromagnetic calorimeter and it is instrumented and read out separately. As there are approximately 0.7 radiation lengths of material in front of it, the energy released in this layer is included in the electromagnetic-cluster shower energy.

Electrons entering the plug calorimeters have reduced geometrical acceptance in the central tracker for $|\eta_{det}| > 1$, which vanishes at $|\eta_{det}| \approx 1.5$. However, the silicon tracker has good coverage in the forward region, which is exploited with a calorimetry-seeded tracking algorithm denoted as "Phoenix." The electron acceptance of this algorithm is roughly 90% to $|\eta_{det}| = 2.4$ and decreases beyond that value but does not vanish. With this algorithm, the track helix in the magnetic field is specified by the position of the $p\bar{p}$ collision vertex, the three-dimensional position of the electron in the PES, and the helix curvature. The collision vertex is reconstructed from other tracks in the event. The curvature is derived from the E_T of the shower in the electromagnetic calorimeter. Two potential helices are formed, one for each charge. The algorithm projects each helix into the silicon tracker to initialize the track reconstruction. If both projections yield valid tracks, the higher-quality one is selected. Depending on its vertex location along the beam line, a track traverses up to eight layers of silicon, of which the track reconstruction uses the outer seven layers. The innermost layer has significant electronic noise and is not used. Phoenix tracks selected for the asymmetry measurement are required to traverse at least three layers and have at least three silicon signals. For the high-E_T electrons from γ^*/Z-boson decays, 85% of the electrons traverse four or more layers for an average tracking efficiency of about 80%.

An electron candidate in a plug calorimeter must have a shower cluster of towers within the electromagnetic calorimeter and an associated signal in the PES detector. The transverse and lateral profiles of the shower cluster are required to be consistent with those obtained from test-beam

electrons. The transverse profile is evaluated in a 3×3 detector-tower grid centered on the highest-energy tower. The goodness-of-fit χ^2 between this profile and the expectation based on the shower-centroid location in the PES detector is denoted by the quantity $\chi^2_{3\times3}$. The longitudinal profile is measured using $E_{\mathrm{HAD}}/E_{\mathrm{EM}}$. Neither a track P_{T} nor an E/P selection requirement is applied because the reconstruction method correlates the track momentum to the calorimeter energy. Charge-misidentification rates of Phoenix tracks increase significantly with increasing $|\eta_{\mathrm{det}}|$ values because the path lengths of the charged particles within the transverse plane of the magnetic field decrease from 129 to 23 cm. The transverse displacements of particles at the track-exit radii of the PES detector relative to the trajectories of particles in the absence of a magnetic field vary quadratically with the path length. The position resolutions are approximately 1.2 mm.

As electrons from $W \to e\nu$ decays originate from the $p\bar{p}$ collision vertex, tracks are required to have impact parameters (d_0), defined as transverse distances of closest approach to the beam line, consistent with zero. Tracks in the central and plug regions are required to have one or more silicon-detector hits and $|d_0| < 175~\mu m$. These mild requirements are effective for removing unwanted events from the electron sample.

The high-E_{T} leptons from the production and decay of W bosons are expected to be produced in isolation from other particles in the event. Consequently, electron candidates are required to be isolated from other calorimetric activity. The isolation energy, E_{iso}, is defined as the sum of E_{T} over towers within a cone of radius 0.4 in (η, ϕ) surrounding the electron cluster. The towers of the electron cluster are not included in the sum. For central-electron candidates, the isolation requirement is $E_{\mathrm{iso}}/E_{\mathrm{T}} < 0.1$; and for plug-electron candidates, it is $E_{\mathrm{iso}} < 4$ GeV.

As the offline-electron sample contains central electrons from the γ^*/Z-production, the following criteria are applied to reduce the fraction of such electrons. These criteria improve the efficiency of event processing over the large number of events in the sample but do not affect the asymmetry measurement. Events with two or more electrons with $E_{\mathrm{T}} > 18$ GeV and $\not{E}_{\mathrm{T}} < 12.5$ GeV are identified. However, the isolation and $E_{\mathrm{HAD}}/E_{\mathrm{EM}}$ requirements are not applied. Electron pairs from the production of γ^*/Z bosons are identified following Ref. [43], and pairs with invariant masses larger than 40 GeV/c^2 are removed.

For central electrons, the selection criteria have an overall efficiency of about 85% and result in a high-quality sample of high-E_{T} electrons. However, the criteria for the plug region result in a sample with significant background, whose level varies significantly with the topology of the reconstructed track in the silicon detector. Track- and electron-quality are combined and made more stringent depending on the background fraction of the track topology. Details are presented in Appendix. These more

stringent criteria result in a sample whose size is 18% smaller but whose quality is vastly improved. Overall, the selection efficiency for plug electrons is about 60%. After the application of the event selection criteria of Sec. V C, the purities of the central- and plug-electron samples are similar.

C. Event selection

For the asymmetry measurement, events are required to have high missing E_{T} and a single high-E_{T} electron. Electrons are accepted if detected in either the central or plug calorimeters with the following conditions:

(1) Central electrons
    (a) $E_{\mathrm{T}} > 25$ GeV;
    (b) $\not{E}_{\mathrm{T}} > 25$ GeV;
    (c) $0.05 < |\eta_{\mathrm{det}}| < 1.00$.
(2) Plug electrons
    (a) $E_{\mathrm{T}} > 25$ GeV;
    (ii) $\not{E}_{\mathrm{T}} > 25$ GeV;
    (iii) $1.2 < |\eta_{\mathrm{det}}| < 2.8$.

The kinematic variables are based on the energy measured in the calorimeter and on the track direction. Detector pseudorapidity η_{det} is defined with the detector coordinates of its shower-centroid location within the CES or PES detectors. The missing-E_{T} vector of an event, $\vec{\not{E}}_{\mathrm{T}}$, is derived using energy-flow measurements from the calorimeters. It is defined as $-\sum_i E_{\mathrm{T}}^i \hat{n}_i$, where the sum is over calorimeter towers, $\hat{n}_i$ is the unit vector in the azimuthal plane that points from the $p\bar{p}$ collision vertex to the center of the calorimeter tower i, and E_{T}^i is the corresponding transverse energy in that tower.

The electron transverse momentum and the missing E_{T} of the event are combined to form the transverse mass of the boson, M_{T}, defined as $\sqrt{2E_{\mathrm{T}}^e E_{\mathrm{T}}^\nu (1 - \cos \Delta\phi_{e\nu})}$, where E_{T}^e is the transverse energy of the electron, E_{T}^ν the missing E_{T} of the event, and $\Delta\phi_{e\nu}$ the azimuthal angle between them. The small fraction of events with $M_{\mathrm{T}} < 45$ GeV/c^2, which are poorly simulated, is removed.

VI. SIGNAL SIMULATION

Data corrections are obtained using a simulation of the data events. The PYTHIA 6.2 event generator [44] with CTEQ5L [45] PDFs simulates the LO QCD interaction $q\bar{q}' \to W$, along with the initial-state QCD radiation of the colliding quarks via its parton-shower algorithms; decays the boson via the $W \to \ell\nu$ channel; and adds quantum-electrodynamics (QED) final-state radiation (FSR) to the charged lepton. Final-state particles not produced in the hard scattering, referred to as the underlying event (UE), are also simulated. The boson-P_{T} and UE parameters are derived from the PYTHIA configuration PYTUNE 101, a tuning to previous CDF data [44,46,47].

The simulation model for the production and decay of W bosons is weighted to resemble the more precise NLO QCD

calculation based on POWHEG-BOX and NNPDF 3.0 PDFs, described in Sec. II. Three event-weight tables are used to improve the agreement. They are a one-dimensional invariant-mass (M) table with high resolution and a lower-resolution pair of two-dimensional tables in the variables (y_{scl}, M) and (y_{scl}, P_T), where y_{scl} is a scaled rapidity defined as $y_{scl} = y/y_{max}$ with $y_{max} = \ln\sqrt{s/(M^2 + P_T^2)}$. As the correction steps are not independent, they are determined using an iterative procedure. Additionally, the angular distribution of the $\ell\nu$ pairs is adjusted. For this correction, the coefficient functions A_{0-4} of Eq. (3) are implemented as two-dimensional tables in the variables $(y_{scl}, P_T/\sqrt{M^2 + P_T^2})$ for the PYTHIA and POWHEG-BOX distributions,[4] the values of the $\mathcal{N}(\vartheta, \varphi)$ functions are calculated for each event with $A_{5-7} = 0$, and the ratio of the values is the adjustment event weight.

Generated events are first processed by the event simulation, which uses PHOTOS 2.0 to account for QED FSR from promptly decaying final-state hadrons and their decay products [48,49], which is not modeled by PYTHIA. In addition, multiple $p\bar{p}$ interactions are added by PYTHIA. This is followed by the CDF II detector simulation based on GEANT-3 and GFLASH [50]. Standard time-dependent beam and detector conditions are incorporated in the simulation, including the p and $\bar{p}$ beam line parameters; the luminous-region profile; the instantaneous and integrated luminosities per data-taking period; and the calibration of detector elements, which include electronic gains and malfunctions. The simulated events are reconstructed, selected, and analyzed in the same way as the experimental data.

The simulation does not describe kinematic distributions such as the E_T of electrons and the missing E_T of events with sufficient accuracy. Modest adjustments are applied to bring the simulation into agreement with the data.

VII. CORRECTION OVERVIEW

A form of the asymmetry expression [Eq. (4)] which shows the net correction of the $(\epsilon A)^+$ and $(\epsilon A)^-$ terms in the measurement is $(N^+ - \rho N^-)/(N^- + \rho N^-)$, where $\rho = (\epsilon A)^+/(\epsilon A)^-$. The $(\epsilon A)^\pm$ terms are evaluated with the simulation after adjustments are applied to obtain agreement with the data. Efficiencies and energies of electrons, energies and distributions of hadrons, and misidentification rates of the electron charge are suitably adjusted. All corrections, except those for the rates of charge misidentification, are independent of the electron charge.

When the correct charge is assigned to the reconstructed electrons of the simulation, the values of $(\epsilon A)^+$ and $(\epsilon A)^-$

---

[4]The extracted values of A_0 are slightly negative for values of P_T near zero. Offsets are added to these table values so that $A_0 \geq 0$.
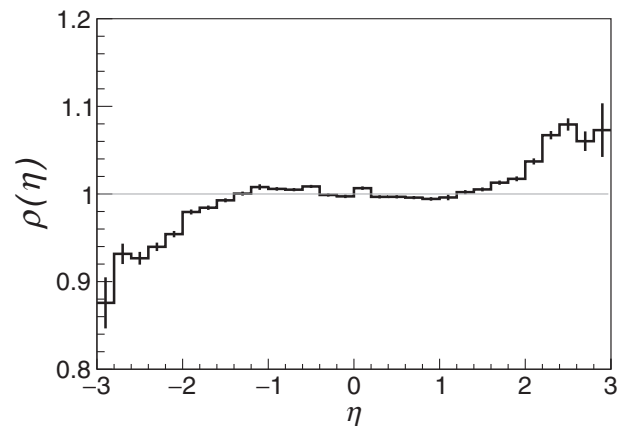

FIG. 4. The ratio $\rho(\eta)$, $(\epsilon A)^+/(\epsilon A)^-$, as a function of η with the correct charge assigned to the reconstructed electrons. The uncertainties shown are statistical.

within an η bin are similar, but vary across η bins. Common portions of, and common uncertainties on, $(\epsilon A)^+$ and $(\epsilon A)^-$, including those from the charge-independent corrections, cancel out to first order in the ratio ρ. Figure 4 shows the ratio as a function of η. Changes in the acceptance ratio with η are due to the E_T distributions of the leptons, which are similar in shape when $|\eta| = 0$ but evolve differently as $|\eta|$ increases in value.

An overview of the corrections and the estimation of the backgrounds in the data is presented in the remainder of this section. Details are presented in Sec. VIII. As many of the charge-symmetric adjustments are influenced by others, the determination process is iterative. Among all corrections, only the charge-misidentification rate of plug electrons has a significant impact on the asymmetry measurement.

A. Electron corrections

Corrections for electrons follow Ref. [43], hereafter referred to as the *ee*-pair analysis. Energy calibrations and efficiency measurements from the *ee*-pair analysis are used as initial calibrations in this work because the kinematic properties of the decay electrons from the production of γ^*/Z and W bosons are similar. Corrections to account for differences in the event environment and selection criteria are applied.

Energy-scale adjustments are applied to the electron energies of both the simulation and the data so that observed energies match the generator level values [51]. The adjustments are applied over the initial corrections. Energy-resolution adjustments are applied to the simulation so that its electron-E_T distributions are in better agreement with those of the data. Additional adjustments are also needed in the simulation to account for relative differences in the amounts of hadronic energy deposited within electron showers.

B. Hadronic corrections

The primary source of hadrons in the simulation is the parton shower associated with the production of the W boson, which approximates the production of hadrons from initial-state QCD radiation. A large fraction of the events contains low-energy parton showers, whose production is nonperturbative. Additional nonperturbative sources of hadrons that are difficult to simulate accurately are multiple interactions and the underlying event. Multiple interactions are independent $p\bar{p}$ interactions within an event, and vary with the instantaneous luminosity. Their prevalence and impact vary. The calorimeter response to hadrons from nonperturbative events is nonlinear and inadequately simulated. Collectively, the hadrons from all sources are denoted as the recoil system of hadrons.

All sources affect the missing E_T and the reconstructed E_T of the electron. Due to the kinematic restrictions on the electron and missing E_T, event acceptances are affected as well. The calibrations of both electron and recoil-system quantities are affected by the spatial distribution of the hadrons relative to the electron.

To orient the spatial distribution of the hadrons, the direction of the recoil system of hadrons with respect to the electron is specified with the parameter $\cos(\Delta\phi_{eX})$, where $\Delta\phi_{eX}$ is the azimuthal angle between the directions of the electron (e) and the recoil system of hadrons (X) produced with the W boson. It is defined in the transverse-momentum frame where the net transverse-momentum of the electron and neutrino is zero. The boost to the frame is defined in terms of the electron $\vec{E}_T$ and event missing $\vec{E}_T$.

Corrections to quantities of the electron and the recoil system of hadrons are evaluated in three $\cos(\Delta\phi_{eX})$ ranges, -1.0 to -0.6, -0.6 to 0.6, and 0.6 to 1.0. As these regions are relative to the electron, they are denoted as the away, transverse, and toward regions, respectively. Figure 5 illustrates the electron-E_T distributions in these regions of $\cos(\Delta\phi_{eX})$. Different kinematic distributions of the leptons are selected by the acceptances of each region. These selections have a secondary effect on the W-boson distributions, and the E_T distributions of the recoil system in these regions are only slightly different. The kinematic separations illustrated in Fig. 5 expose direction-dependent differences of the simulation relative to the data.

Energy-scale corrections are first applied to the energies of the recoil systems of both the data and simulation so that the observed energies are calibrated to the generator-level energies [51]. Additional corrections are then applied to the simulation that account for data-to-simulation differences in the energy and spatial distributions of the hadrons.

C. Backgrounds

Backgrounds total about 5%. They are simulated for the following processes, which produce high-P_T electrons:
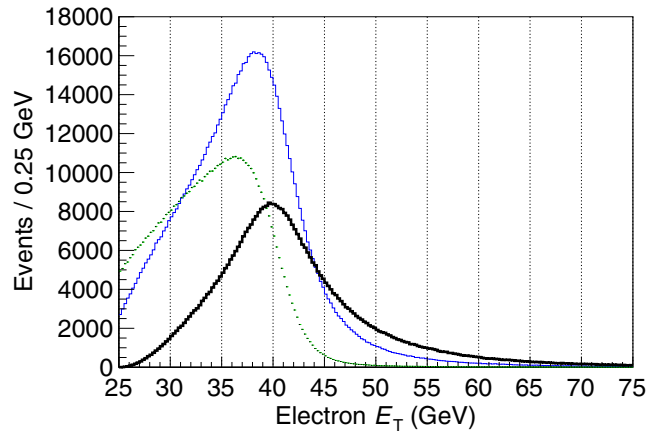

FIG. 5.   Simulated E_T distributions of the away, transverse, and toward regions for the electrons in the plug calorimeter. Distributions for electrons in the central calorimeter are similar. The bold (black) histogram is for the away region, the light (blue) histogram is for the transverse region, and the (green) crosses are for the toward region. Corresponding $\not{E}_T$ distributions follow a similar pattern except that away and toward are reversed because the direction away from the electron is toward the neutrino and vice versa.

$\gamma^*/Z \to ee, \tau\tau$, $W \to \tau\nu$, dibosons (WW, WZ, ZZ), and $t\bar{t}$ pairs. The model of the QCD background is extracted from an experimental data sample independent of the signal sample. Background rates are normalized to the signal rates, and subtracted from distributions of the data.

The fraction of the QCD background in the measurement sample depends on the location of the electron candidate, but overall is under 2%. Events from QCD background are due to parton-parton scattering interactions that result in outgoing partons that fragment into cascades of hadrons called *jets*. A small fraction of jet cascades contains electron candidates. QCD events are not expected to exhibit any $\not{E}_T$, but nonzero values are observed because jets can have reconstructed energies that differ from their underlying energies, even significantly, due to the resolution of the detector or the traversal of hadrons into uninstrumented regions of the detector. However, the number of events with these instrumental effects decreases rapidly with increasing $\not{E}_T$ values.

The amount of QCD background in data is determined via a fit of the QCD model and signal contributions to the $\not{E}_T$ distributions.

D. Charge misidentification

Charge-misidentification rates are significant only in the plug regions. They are accounted for using measurements on e^+e^- pairs with one electron in the central region and the other in the plug region. Event selection follows that of the ee-pair analysis. Central-region tracks, whose charges are well measured, provide the reference charges expected for the plug-region tracks. Rates are position-dependent and measured over small regions of (η_{det}, ϕ). As this

division limits the statistical precision of the rates, the rates are not measured as functions of any other parameters.

VIII. DATA AND SIMULATION CORRECTIONS

A. Event-rate normalizations

The default simulation does not model the trigger and reconstruction efficiencies observed in the data with the desired precision. Event weights based on the efficiencies derived from the ee-pair analysis are used as the initial correction to the simulation. The event weights are ratios of the selection efficiencies observed in data to the simulation versus time, position in the detector volume (denoted henceforth as detector location), and instantaneous luminosity.

As the electron-selection criteria of the $e\nu$-pair analysis are more stringent than those of the ee-pair analysis, an additional correction is determined using the ee-pair data. The criteria of the $e\nu$-pair analysis are applied over those of the ee-pair analysis, and efficiencies calculated for both the data and simulation samples. The efficiency ratio between the data and simulation provides the additional correction.

Changes of the Tevatron-luminosity profile over time are measured using the $e\nu$-pair data and incorporated into the simulation. The distributions of the location of the $p\bar{p}$-collision vertices along the beam line (z_{vtx}) and the number of multiple interactions in an event (n_{vtx}) changed significantly with improvements to the beam current and optics of the Tevatron. Measurements of the z_{vtx} distribution, which has an rms dispersion of about 30 cm, are organized into seven time intervals corresponding to the introductions of major improvements in the Tevatron collider. As η_{det} is a function of z_{vtx}, inaccuracies impact the determination of the acceptance. The n_{vtx} quantity is a measure of the instantaneous luminosity for the event. Measurements of the n_{vtx} distribution are organized into calibration periods.

Another luminosity parameter, denoted as the average instantaneous luminosity, is important for corrections to simulated quantities over long periods of time. This parameter tracks the effects of the beam to the event environment over multiyear periods associated with major changes in the average $\bar{p}$ current circulating within the Tevatron. Two time intervals need to be taken into account by the simulation. The first interval covers calibration periods where the average instantaneous luminosity is relatively low (low-luminosity period), and the second interval covers calibration periods where the average instantaneous luminosity is relatively high (high-luminosity period).

The initial coarse correction is refined toward a better resolution in time, position, and luminosity using the events of the $e\nu$-pair analysis. These finer extensions are separate for the events with central-region and plug-region electrons, and use event-count ratios between the data and simulation as event weights. All corrections are functions of n_{vtx}. Some are functions of the low- or high-luminosity period. Corrections for detector-location dependencies are functions of $|\eta_{\mathrm{det}}|$. For the central region, the location correction accounts for data-to-simulation differences of the efficiencies across the CES detector. For the plug region, the correction accounts for differences of both the efficiencies across the PES detector and the position-dependent response of EM-calorimeter towers.

B. Selection quantities

The simulated distributions of isolation energy E_{iso} and the plug-electron $\chi^2_{3\times3}$ are adjusted to improve the agreement with data. Isolation distributions are used in the analysis of QCD backgrounds. For electron candidates in the plug region, the adjustments are important because the criteria for their selection detailed in Appendix are more stringent.

C. Electron-energy corrections

The initial corrections to the default calibrations use electron pairs where one is detected in the central calorimeter and the other in the plug calorimeter. Corrections to the energy scale and resolution are functions of $(\eta_{\mathrm{det}}, \phi)$. The scale is also dependent on the low- or high-luminosity period. The initial corrections also account for the extra energy in an electron shower from the underlying event and multiple interaction sources as an average correction over all event topologies. Adjustments to these energy calibrations are derived for the $e\nu$-pair analysis.

Electron-energy corrections specific to the $e\nu$-pair analysis are implemented in four steps. The first is the calibration of the electron energy at the reconstruction level of the simulation to the event-generator level [51]. Next, the energy scale of the data is aligned with that of the simulation. The third step accounts for small but location-dependent differences between the simulation and the data in the amounts of shower energy from hadronic sources within electron showers. The $\cos(\Delta\phi_{eX})$-dependent offsets of the simulated electron-E_{T} distributions are corrected relative to the data. Finally, the energy resolution of the simulation is adjusted to improve agreement with the data.

The calibration of the energy scale of the simulation begins by associating the reconstruction-level electron with its generator-level counterpart. Then the electron and its companion electrons and photons from QED FSR are clustered around the seed tower as in the electron reconstruction. The seed tower is based on the reconstructed electron, and the projection from the $p\bar{p}$ collision vertex to the tower is achieved by extrapolating the track helix. The calibration is derived from the distribution of the ratio of the reconstruction-level energy E_{rec} to the clustered energy at the generator level E_{clus}. In the vicinity of its peak, which occurs at ratios of about 1.0, the distribution is approximately Gaussian. The energy scale is adjusted to make it peak at 1.0. There are $|\eta_{\mathrm{det}}|$-dependent adjustments

of about 0.5% or less, with the larger shifts being in the plug region.

The electron-E_T distributions are used for the alignment of the energy scale of the data with that of the simulation. For most EM-calorimeter towers, the data distributions agree with those of the simulation without any adjustments. The overall uncertainty of the energy scale based on the χ^2 between the data and the simulation is $\pm 0.04\%$.

To measure the energy shifts between the simulation and the data due to the hadrons, events are separated into classes according to whether the electron is detected in the central or plug region, instantaneous luminosity, low- or high-luminosity period, n_{vtx}, and the region of $\cos(\Delta\phi_{eX})$. These groups are denoted as "standard-calibration groups." The shapes of the electron-E_T distributions for each $\cos(\Delta\phi_{eX})$ region are similar to those shown in Fig. 5. Along the rising and falling edges about the peaks of the distributions, small offsets separating the simulated and experimental data are measured. Observed offsets are of order 50 (100) MeV for electrons detected in the central (plug) calorimeter, and vary in magnitude and sign.

The model for the energy-resolution of the simulation is $\sigma^2 = c_0^2 E + c_1^2 E^2$, where σ is the resolution, E the electron energy, c_0 the sampling term, and c_1 the miscalibration or constant term. The sampling term, calibrated with test-beam data, is part of the default detector simulation. Additional adjustments are applied to the constant terms of both central- and plug-region electrons so that the electron-E_T distributions agree better with the data.

Simulated electrons of the central region have a slightly broader E_T distribution around the peak than in the data. To reduce mismodeling, the reconstructed energy E_{rec} in the simulation is modified on an event-by-event basis using $E'_{rec} = E_{clus} - f_{rms}(E_{clus} - E_{rec})$, where E'_{rec} is the adjusted value and f_{rms} a parameter. As the $E_{clus} - E_{rec}$ term gives the fluctuation of the reconstructed energy from its generator-level value, the f_{rms} parameter rescales the rms of the fluctuations. The optimization of f_{rms} constrained by the data yields $f_{rms} = 0.87 \pm 0.03$.

Simulated electrons of the plug region have a narrower E_T distribution around the peak than in the data. This is broadened on an event-by-event basis by incorporating Gaussian fluctuations to the energies that effectively increase the constant term c_1 beyond its default value of 0.01. The adjustment is a function of the $|\eta_{det}|$ coordinates of calorimeter towers and the $p\bar{p}$-interaction count n_{vtx}. Adjusted values for c_1 range from 0.021 to 0.056 for increasing values of $|\eta_{det}|$ and n_{vtx}. The uncertainty of the c_1 terms is estimated by rescaling all terms with a uniform factor, propagating the effects to the E_T distributions, then comparing them to the data. This results in a relative uncertainty of $\pm 4\%$ on the constant terms.

Figure 6 shows the E_T distributions of electrons in the central and plug regions after all corrections
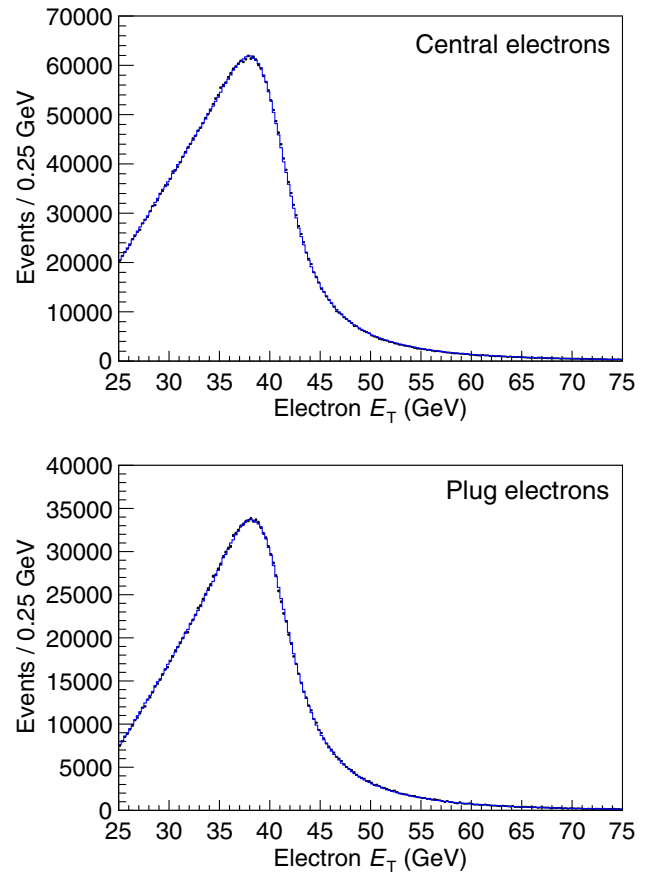

FIG. 6. Background-subtracted E_T distributions of electron candidates in the central and plug regions. The crosses are the data and the solid histogram is the simulation. The comparison between the data and the simulation for electron candidates of the central (plug) region yields a χ^2 of 373 (317) per 200 bins.

are applied, including the hadronic corrections of Secs. VIII E–VIII F and the subtraction of backgrounds described in Sec. VIII G. All corrections need to be applied because of the correlations among them. Adjustments based on the $\cos(\Delta\phi_{eX})$ parameter significantly reduce the biases affecting different regions of the simulated-E_T distribution relative to the data.

Figure 7 shows the corresponding η distribution of the electrons. The valley structures of the distribution reflect the nonfiducial regions in the central calorimeter ($|\eta| \sim 0$) and between the central and plug calorimeters ($|\eta| \sim 1.1$). Electron-E_T distributions in η subregions covered by the central and plug calorimeters, $|\eta|$ values above and below 0.5 for the central calorimeter and $|\eta|$ values above and below 1.6 for the plug calorimeter, are adequately simulated. The shapes of the E_T distributions of the central (plug) subregions are similar to those of the central (plug) region in Fig. 6. Comparisons between the data and the simulation for the electron candidates of the four subregions yield statistical-χ^2 values ranging from 360 to 550 for 200 bins.
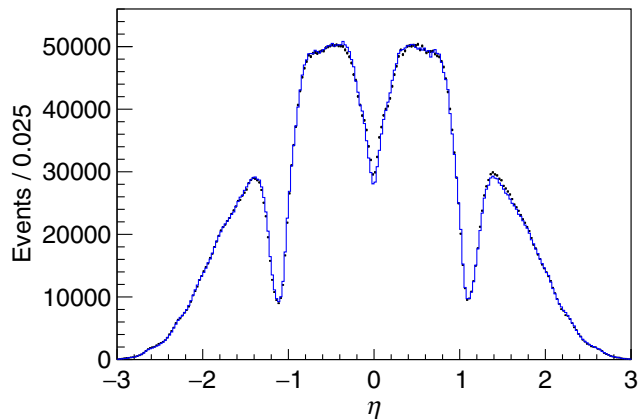
FIG. 7. Background-subtracted η distribution of the electron candidates used in the measurement of the asymmetry. The crosses are the data and the solid histogram is the simulation. All corrections have been applied.

D. Recoil system of hadrons

The momenta of the W boson ($\vec{P}_\mathrm{T}^W$) and of the recoil system of final-state particles directly associated with the boson production ($\vec{P}_\mathrm{T}^X$) balance each other in the transverse plane of an event so that $\vec{P}_\mathrm{T}^X = -\vec{P}_\mathrm{T}^W$. The transverse energy of the recoil system observed in the detector, denoted by $\vec{E}_\mathrm{T}^{X(\mathrm{obs})}$, is the quantity $-\vec{\slashed{E}}_\mathrm{T} - \vec{E}_\mathrm{T}^e$, where $\vec{E}_\mathrm{T}^e$ represents the uncorrected contribution of the electron shower to the missing-E_T term.

The observed recoil $\vec{E}_\mathrm{T}^{X(\mathrm{obs})}$ is a combination of the products of the hard collision producing the W boson and of the other activity in the event such as the underlying event and multiple interaction sources. In the QCD parton model, the outgoing parton from the hard collision recoiling against the W boson fragments into a jet. At large values of the parton P_T, the fragmentation results in a collimated jet of particles in the detector. Energetic final-state partons with sufficiently low values of P_T fragment into jets where a fraction of the particles enter the beam hole. Hadrons from softer nonperturbative partons are distributed more broadly.

The calorimeters are calibrated so that particles that undergo electromagnetic showering have $E/P \approx 1$. However, the response to a hadronic cascade is intrinsically different from an electromagnetic cascade. In the simulation, the response of the calorimeters to jet particles is based on the observed responses from single particles in test beams and collider data [52]. The measured responses of particles with momenta down to 0.5 GeV/c are incorporated into the GFLASH model of the calorimeter response. For a 2 GeV/c hadron, E/P equals about 0.65 and increases with the particle momentum. As jets typically consist of many low-momentum particles, the observed energy of the jet in the calorimeters is lower than the momentum of the underlying particles.

For clustered jets, corrections to transform the jet response of the calorimeters to the momentum of the underlying jet of particles have been determined [52]. These jet corrections are validated using events with γ^*/Z-bosons produced in association with jets, where the γ^*/Z bosons are reconstructed from electron and muon pairs. The transverse momentum of the lepton pair serves as the reference value for that of the jet to be corrected. The resulting distributions of the difference between the transverse momenta of the boson and of the jet are peaked close to zero. The shapes of the distributions are also similar.

The energy scale for the recoil system, which is unclustered, is investigated using the simulation and the transverse momentum of the system from the event generator. With the default simulation of the detector, the bias $P_\mathrm{T}^X - E_\mathrm{T}^{X(\mathrm{obs})}$ increases approximately linearly with P_T^X in the region above 30 GeV/c. Below 30 GeV/c, the detector response to the particles of the recoil system is nonlinear. Increasing the energy scale by a factor of 1.175 yields a $\mathcal{O}(1)$ GeV bias, which is approximately constant to about $\pm 15\%$ for the region above 30 GeV/c.

The energy-scale result of the recoil-system analysis is similar in characteristics and values to the jet-energy-scale calibration result of Ref. [52] for clustered jets. The recoil system in data with electron pairs from γ^*/Z-boson decays provides a test of the scale factor. The recoil-system bias of electron-pair events is defined as $P_\mathrm{T}^{ee} - E_\mathrm{T}^{X(\mathrm{obs})}$, where P_T^{ee} is the transverse momentum of the pair. As in the simulation, applying a recoil-energy scale of 1.175 also yields a bias that is approximately constant for the region above 30 GeV/c.

E. Hadronic calibrations

Calibrations associated with the recoil system of hadrons in the detector are complex because the hadrons are spread across a large region of the calorimeter, the calorimeter response is nonlinear, and there are sizeable regions with cracks in the calorimeter coverage where the response of the simulation is inadequate [52]. Position-dependent jet corrections are not applied by default in the missing-E_T calculation.

The calibration strategy is to first fix the energy scale of the recoil system in the data to 1.175, then adjust the corresponding energy scale in the simulation so that the response matches that of the data for events with large-$E_\mathrm{T}^{X(\mathrm{obs})}$ values. For the remainder of the calibration, events are partitioned into the standard-calibration groups. The offsets between the simulation and data for the x and y components of the recoil-E_T vector and the shapes of the recoil-E_T distributions are corrected.

To determine the energy-scale correction factor of the simulation relative to the data, events with $E_\mathrm{T}^{X(\mathrm{obs})} > 30$ GeV are selected for both the simulation and the data.

With this selection, a scale change alters the profiles of all simulated E_T distributions. The simulation scale is expressed as the product of the data scale and a variable relative scale that is adjusted using events from the away region of $\cos(\Delta\phi_{eX})$, where the electron and recoil system are approximately opposite in azimuth. As the energies of the electron and recoil-system of hadrons are expected to balance, a scale misalignment appears as an energy offset between the electron-E_T distributions of the data and the simulation. These distributions are similar to the away-region distribution of Fig. 5, but peaked near 55 GeV. In order to minimize contamination from multiple inter-actions, only the events with $n_{vtx} = 1$ are used in the adjustments. For the low- and high-luminosity periods of the central-region events, the relative-scale values after the alignments are 0.959 ± 0.006 and 0.958 ± 0.006, respectively. For the plug-region events, they are 0.943 ± 0.007 and 0.930 ± 0.007, respectively. These values are used on all n_{vtx} categories.

The distributions of the x and y components of the recoil-E_T vector are centered near the origin, and their offsets from the origin are 1 GeV or less in magnitude, with magnitudes typically increasing with n_{vtx}. Differences between the offsets of the data and the simulation are measured and applied as event-by-event corrections in the simulation. Next, the recoil-E_T distributions of the simu-lation are adjusted to match those of the data using event weights that preserve normalizations. After these adjust-ments, data-to-simulation differences in the $\cos(\Delta\phi_{eX})$ distributions remain. They vary with $\cos(\Delta\phi_{eX})$, and do not exceed $\pm 10\%$ for the distribution with the largest difference. The shapes of the simulated-$\cos(\Delta\phi_{eX})$ distri-butions are adjusted using event weights. These adjust-ments modestly improve the agreements between the data and simulation in the recoil-E_T distributions, but have a large impact on the $\not{E}_T$ distributions in conjunction with their effects on the electron-E_T distributions.

Figure 8 shows the $E_T^{X(obs)}$ distribution of the recoil system for electrons in the central and plug regions after all corrections, including those for the missing-E_T of Sec. VIII F and the subtraction of backgrounds described in Sec. VIII G, are applied. The simulated distributions are expected to similar to those of the data.

F. Missing-E_T corrections

The corrected-$\not{E}_T$ vector of an event is a composite object obtained from the calibrated-$E_T^{X(obs)}$ vector by incorporat-ing the contribution of the calibrated-E_T vector of the electron. Corrections to the electron energy and to the distribution of the electron relative to the recoil system of hadrons tend to have a significant impact on the missing-E_T of events. The impact is large because the E_T of the recoil system of hadrons is typically smaller than that of the electron and thus the electron shower is a dominant component of all energy deposited in the calorimeters.
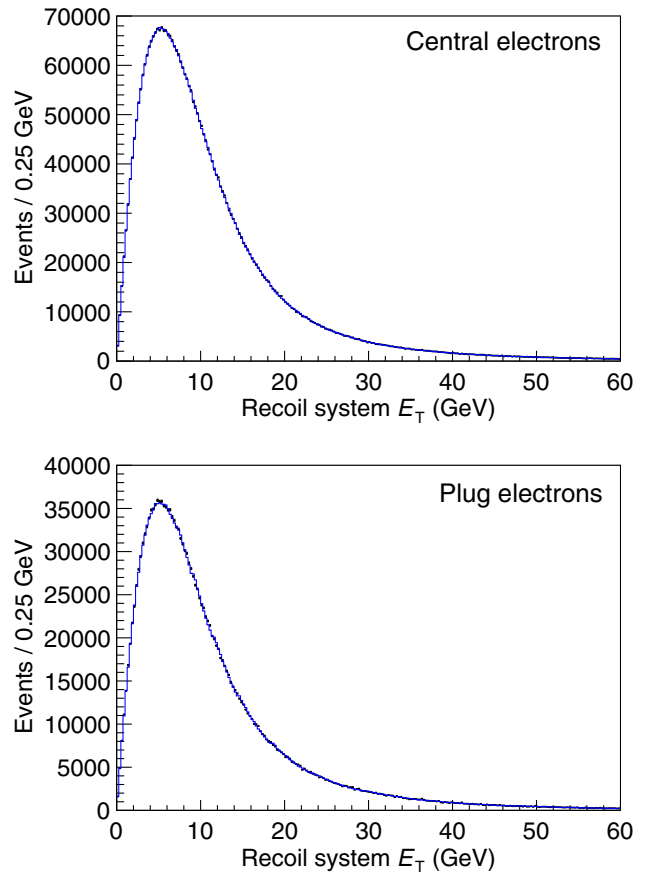

FIG. 8. Background-subtracted $E_T^{X(obs)}$ distributions for elec-tron candidates in the central and plug regions. The crosses are the data and the solid histogram is the simulation. The compari-son between the data and the simulation for electron candidates in the central (plug) region yields a χ^2 of 256 (402) per 240 bins.

Plug-region events of the high-luminosity period show small missing-E_T differences between data and simulation at values greater than 65 GeV. The simulated efficiency of the underlying electron in this region is slightly lower than in the data as the default normalization and efficiency are from optimizations over all events and are not specific to the high-E_T conditions. Adjustments are applied to the simulated-electron efficiency of the events to mitigate the differences. The integral of the correction amounts to under 0.1% of all events.

Figure 9 shows the $\not{E}_T$ distributions for electrons in the central and plug regions after all adjustments are applied to the underlying quantities. The subtraction of backgrounds discussed in Sec. VIII G is also applied.

Figure 10 shows the transverse mass (M_T) distributions for electrons in the central and plug regions after all adjustments are applied to the underlying quantities, including the subtraction of backgrounds discussed in Sec. VIII G. The M_T distribution reflects the azimuthal angular distribution between the electron and missing-E_T quantities of events.
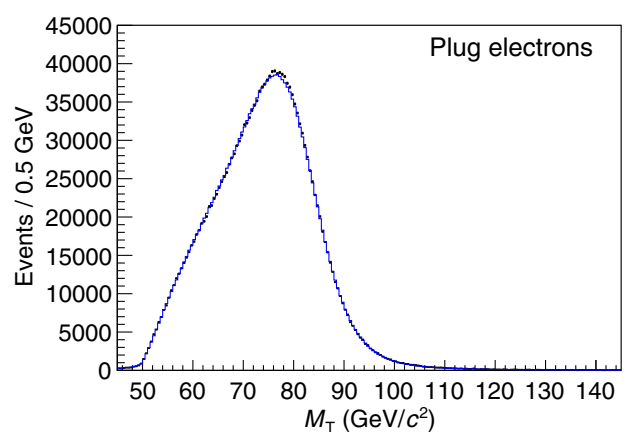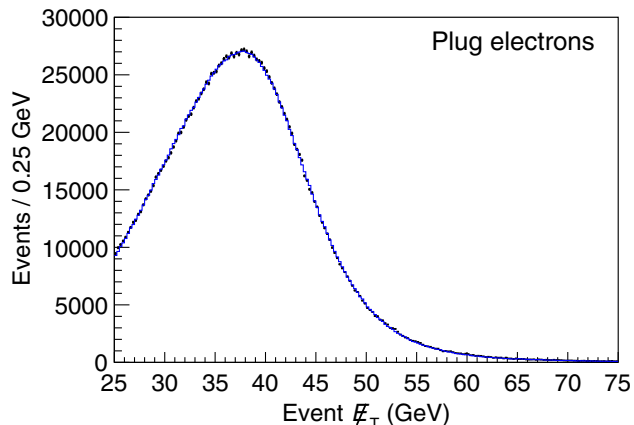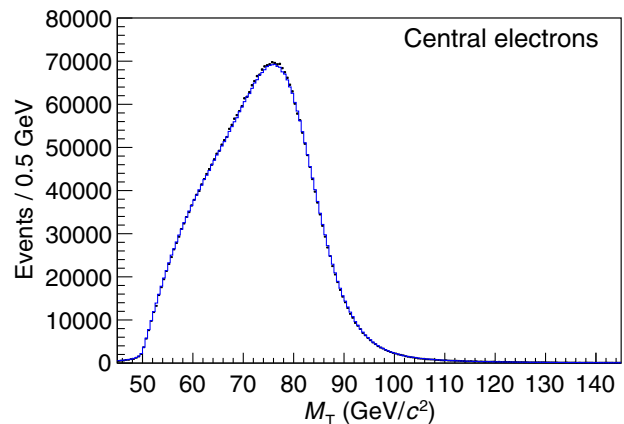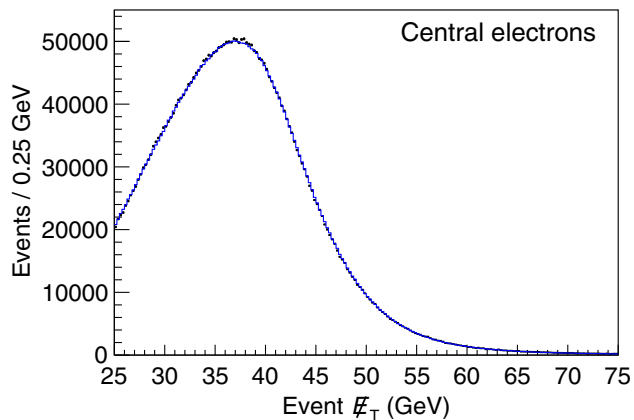
FIG. 9. Background-subtracted $\not{E}_T$ distributions for electron candidates in the central and plug regions. The crosses are the data and the solid histogram is the simulation. The comparison between the data and the simulation for electron candidates in the central (plug) region yields a χ^2 of 260 (310) per 200 bins.

FIG. 10. Background-subtracted M_T distributions for electron candidates in the central and plug regions. The crosses are the data and the solid histogram is the simulation. The comparison between the data and the simulation for electron candidates in the central (plug) region yields a χ^2 of 384 (402) per 200 bins.

G. Backgrounds

Backgrounds from the central and plug regions are determined separately. Backgrounds from the processes $\gamma^*/Z \to ee$, $W \to \tau\nu$, $\gamma^*/Z \to \tau\tau$, dibosons (WW, WZ, ZZ), $t\bar{t}$ pairs, and QCD multijets are considered.

Events produced by the $\gamma^*/Z \to ee$ process can occasionally have significant amounts of missing-E_T, similar to QCD events. Electron showers within uninstrumented portions of the detector can result in significant amounts of missing E_T being indicated. However, the number of such events is relatively small compared to that from the $W \to e\nu$ process.

The QCD-background sample is derived from the data. Other backgrounds are derived from PYTHIA [44] samples that are processed with the detector simulation and in which the integrated luminosity of each sample matches the data. The diboson and $t\bar{t}$ samples are inclusive and their normalizations use total cross sections calculated at NLO [53] and next-to-next-to-leading order [54], respectively. The $W \to \tau\nu$ and $Z \to \tau\tau$ sample normalizations use the total cross sections from PYTHIA multiplied by the 1.4 ratio

of the NLO-to-LO cross sections. The $\gamma^*/Z \to ee$ sample is the signal sample of the ee-pair analysis [43], and data-constrained normalizations derived therein are utilized. Sample normalizations as mentioned above are referred to as the default normalizations. All normalizations are implemented as event weights. This allows background events to be subtracted from (added to) event distributions via the use of negative (positive) weights.

Candidates of the QCD sample are a subset of the events that fail the event-selection criteria. Events in this sample fail the E_{HAD}/E_{EM} criterion, but satisfy all other electron-identification criteria except the isolation criterion. This subset definition enhances the fraction of QCD events, and, limits the events to those whose kinematic distributions are closer to those of the QCD events within the signal sample due to the similarity of the selections. For the background in plug-region events, the additional requirement on the transverse-shower shape described in Appendix is removed because it severely limits the size of the sample.

The QCD sample includes events from non-QCD processes with high-E_T electrons. These events are modeled
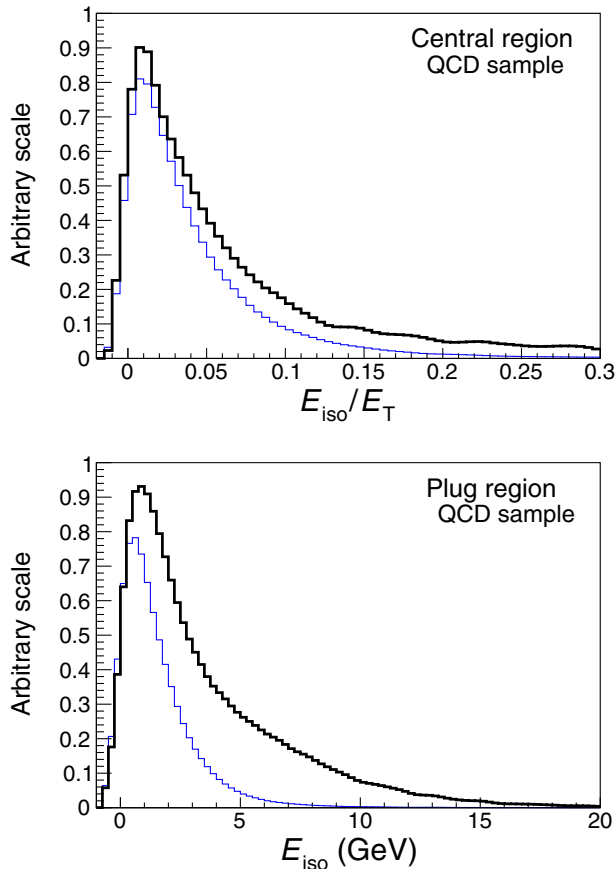
FIG. 11.　Shape of the isolation distributions of events in the central and plug regions of the QCD sample. The bold (black) histogram is the data and the lighter (blue) histogram is the expected contribution of the non-QCD processes.

using the same PYTHIA samples of the $W \to e\nu$ and background processes. However, events are required to pass the selection criteria for the QCD sample. Most of the events are from the $W \to e\nu$ process.

Figure 11 illustrates the shape of the isolation distributions from the QCD sample for events of the central and plug regions. Also shown is the expected contribution of the non-QCD component, normalized relative to the QCD component. To normalize the non-QCD component of the sample to the QCD component, events are split into two disjoint sets based on the isolation energy of the electron candidate. These collections are denoted as the tight- and loose-isolation sets. Events with central-region candidates having $E_{iso}/E_T < 0.05$ and events with plug-region candidates having $E_{iso} < 2$ GeV are assigned to the tight-isolation set. Unassigned events form the loose-isolation set.

The sole purpose of the tight-isolation set is to provide the normalizations of the non-QCD processes within the QCD sample. The QCD events of the loose-isolation set are used as the model for the QCD background within the signal sample. Normalizations of the various components

in the QCD samples are determined for each standard-calibration group.

Normalizations for the non-QCD processes are derived using the $\not{E}_T$ distribution of events. Events from QCD processes are concentrated in the region with $\not{E}_T$ smaller than approximately 35 GeV. At higher values, $e\nu$ events from the production of W bosons dominate while the contribution from QCD production is small. A single scale applied to the default normalizations of the non-QCD processes is adjusted so that the simulated distribution in the region above 35 GeV is in better agreement with that of the data. As the loose-isolation set includes events from non-QCD processes, their contribution is subtracted to yield the model of the QCD background within the signal sample.

All events of the model are used for the subtraction of the QCD background from the signal sample, i.e., the isolation requirement of the signal sample is not applied. Normalizations for the background are derived using the $\not{E}_T$ distributions of signal events for the data and simulation. The event yields of the simulation and QCD background are adjusted in a two-parameter fit so that their sum matches that of the data.

Backgrounds from QCD processes are larger in the plug region and suffer from insufficiently accurate predictions. To improve the agreement between the observations and the predictions, events with electron candidates in the plug region are subdivided further into smaller groups based on the additional selection criteria for electrons described in the Appendix, and the levels of the QCD background therein determined.

Examples of the QCD backgrounds in the missing-E_T distributions of plug-region electrons from the high-luminosity period and $n_{vtx} = 2$ for the away, transverse, and toward regions of $\cos(\Delta\phi_{eX})$ is shown in Fig. 12, where only the larger backgrounds are shown to reduce the overlap of histograms. Distributions for electron candidates in the central calorimeter are similar.

The toward-region distribution is suppressed at low missing-E_T values because most of its events have geometries where the missing-E_T vectors are in opposite directions relative to those of the electron and recoil systems. As the QCD background in this region is small, the data inputs to the fit do not constrain the QCD normalization. Consequently, the normalization is fixed to a value determined from an extrapolation that uses the $\cos(\Delta\phi_{eX})$ distribution of the QCD background, which decreases exponentially as the value of $\cos(\Delta\phi_{eX})$ increases. All toward-region distributions are similar and treated the same way.

Plug-region events of the high-luminosity period have small differences between data and simulation in the electron-E_T distribution for $E_T > 65$ GeV. In this region, the predicted amount of QCD background is large, exceeding the signal at $E_T > 80$ GeV. Adjustments are applied to
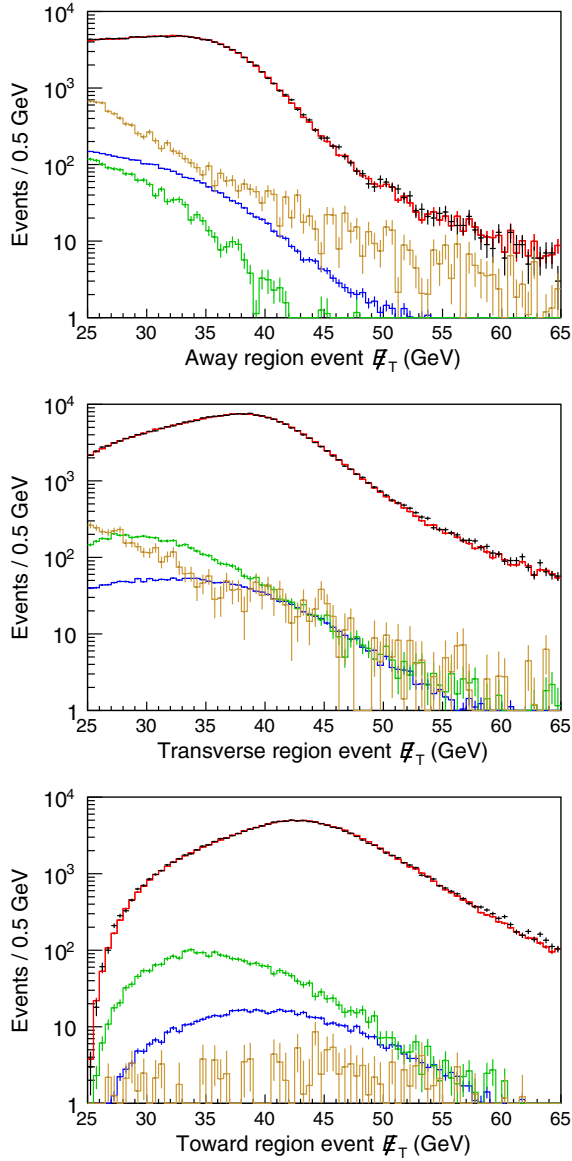
FIG. 12. $\not{E}_T$ distributions for electron candidates in the plug calorimeter from the high-luminosity period with $n_{vtx} = 2$ in the $\cos(\Delta\phi_{eX})$ regions. The (black) crosses are the data, the (red) histogram overlapping the data is the simulation with all backgrounds, and the lower histograms are the backgrounds for QCD (brown), $\gamma^*/Z \to ee$ (blue), and $W \to \tau\nu$ (green). For the away region, the backgrounds from top to bottom are QCD, $\gamma^*/Z \to ee$, and $W \to \tau\nu$. For the toward region, the order is reversed. For the transverse region, the backgrounds from top to bottom along the y axis are QCD, $W \to \tau\nu$, and $\gamma^*/Z \to ee$.

TABLE I. Background composition. Relative uncertainties of the QCD backgrounds are 12% for the central-region electrons and 6% for the plug-region electrons. All simulated backgrounds have a 6% relative uncertainty associated with the integrated luminosity [55] with the exception of the $\gamma^*/Z \to ee$ background, which is well constrained by the electron-pair data [43].

	Background fraction (%)	
Component	Central region	Plug region
$W \to \tau\nu$	1.78	1.62
QCD	0.91	1.98
$\gamma^*/Z \to ee$	1.09	0.96
$\gamma^*/Z \to \tau\tau$	0.29	0.35
Diboson	0.14	0.13
$t\bar{t}$	0.08	0.04

individual contributions from the various background processes, is shown in Fig. 13 for events in the central and plug regions.
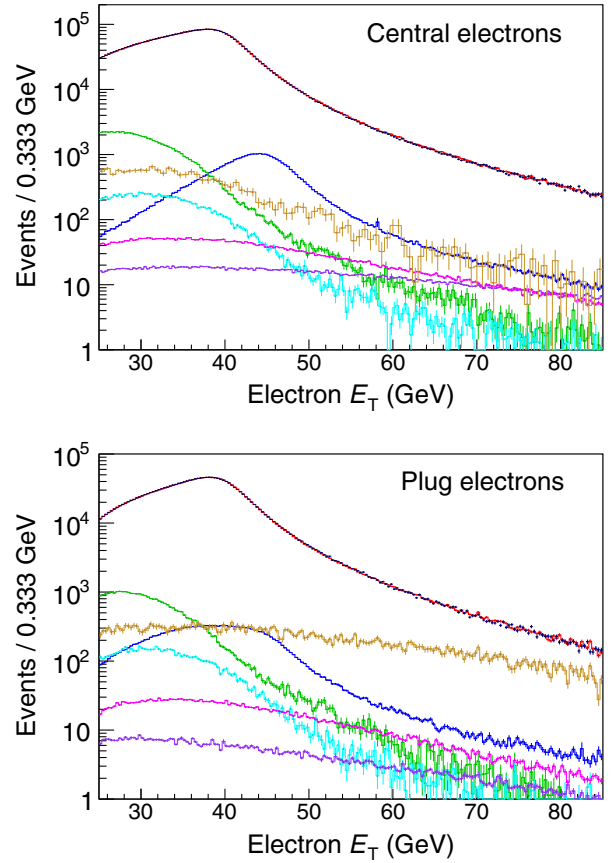

FIG. 13. E_T distributions of electrons in the central and plug regions. The data are the crosses (black) and the simulation with all backgrounds is the histogram (red) overlapping the data. The individual backgrounds are the lower histograms, and from the top to bottom along the left edge of the plot they are the $W \to \tau\nu$ (green), QCD (brown), $\gamma^*/Z \to \tau^+\tau^-$ (cyan), $\gamma^*/Z \to ee$ (blue), diboson (magenta), and $t\bar{t}$ (purple) contributions. For plug electrons, $\gamma^*/Z \to ee$ (blue) peaks around 40 GeV.

the QCD-background shape to mitigate the differences. The integral of the correction amounts to 0.1% of all events.

The data samples consist of approximately 3 819 000 events for the central region and 2 003 000 events for the plug region. Table I lists the background composition. The fully corrected electron-E_T distributions, including the

H. Charge-misidentification rates

The rates of charge misidentification for central-region tracks are small and are due to interactions of the electrons with the material in the tracking volume. For tracks associated with plug electrons, the misidentification rates are significant, and increase with $|\eta_{det}|$. No charge bias is detected in the track reconstruction. The charge bias and rates of charge misidentification are studied using e^+e^- pairs from γ^*/Z-boson production. The event selection follows the *ee*-pair analysis except that the track requirements of the *eν*-pair analysis are applied.

For the study of the charge bias of plug-region electrons, the dielectron masses are limited to the range 66 to 116 GeV/c^2. Pairs with one electron in the central region and the other in the plug region are used to determine the charge bias for plug electrons. The central-region electron provides the reference charge for the measurement. A positive charge is assigned to the plug electron if the central-electron charge is negative, and vice versa. The bias is measured using the asymmetry $A_b = (N^+ - N^-)/(N^+ + N^-)$, where $N^\pm$ is the number of plug electrons with $\pm$ charges. As a function of $|\eta_{det}|$, the asymmetry of plug electrons is consistent with zero and integrates to -0.001 ± 0.002.

For the measurement of the rates of charge misidentification, the dielectron masses are limited to exceed 40 GeV/c^2. For pairs where both electrons are in the central region, the electron with the largest E_T provides the reference charge for the measurement of the misidentification rate of the opposing electron. For pairs where one electron is in the central region and the other is in the plug region, the central-region electron provides the reference charge for the measurement of the misidentification rate of the plug-region electron.

Rates of charge misidentification are measured on a 44×8 (η_{det}, ϕ) grid which reflects the transverse segmentation of the calorimeter towers. Subdivisions along the η_{det} direction correspond to the 44 azimuthal rings of towers, numbered from 0 to 43. The low (high) edge of ring 0 (43), which is adjacent to the beam line, is located at $\eta_{det} = -3.5$ (3.5); however, these rings are not in the fiducial region. Subdivisions along the ϕ direction correspond to a 45° section of adjacent towers in a ring. Each subdivision in ϕ is denoted as a sector.

The sector subdivisions along the ϕ direction match the underlying wedge structure of the PES detector, which provides the exit point for track finding in the plug region. Each PES wedge is aligned as a single unit with the track detectors of the central region.

The rate of misidentification, $m^\pm$, is the fraction of observed (simulated) particles with expected (known) charge $\pm$ reconstructed with the wrong charge. Figure 14 illustrates the average misidentification rates of electrons and positrons, where the tower rings are drawn at their locations in η_{det} space. Zones with null rates are not in the fiducial region. In the plug region ($|\eta_{det}| > 1.1$), rate
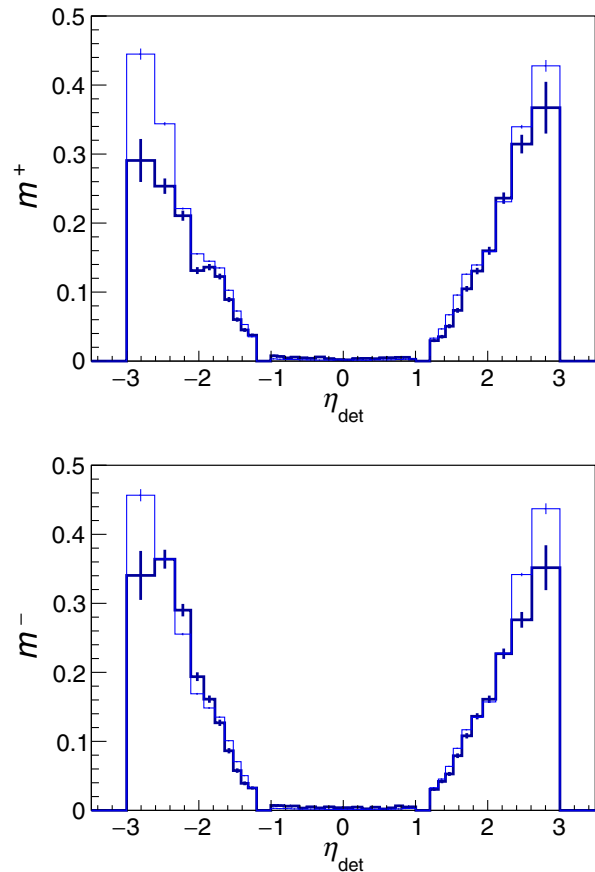

FIG. 14. Charge-misidentification rates $m^\pm$ averaged over the sectors of a ring, versus η_{det}. The bold (black) histogram is for the data, and the lighter (blue) histogram for the simulation.

variations among the ϕ-sectors of a ring are significant for both the data and simulation. The data rates include the effects from discrepancies between the true orientation of each PES wedge and that specified by the alignments. For the simulation, the alignments are exact.

For the individual sectors of ring 1 (42) towers near the beam line, the numbers of events available for the rate measurements range from tens down to a handful. The quality of the measurements is inadequate. Consequently, a rate based on the combined events of rings 1 and 2 (42 and 41) within the same PES wedge is used. The rates of these rings are correlated because they are adjacent in the same strip detector. However, there are η_{det} dependencies as shown in Fig. 14. To account for these dependencies, the combined rate of rings 1 and 2 (42 and 41) of a PES wedge is scaled by the ratio of the integrated rate over all sectors of ring 1 (42) to that of the combined rate integrated over all sectors. The scaled results are consistent with the original ring 1 (42) rates.

I. Charge-misidentification corrections

The numbers of events with correctly and incorrectly reconstructed charges for the simulation are given by

$N_t^{\pm}(1 - m^{\pm})$ and $N_t^{\pm}m^{\pm}$, respectively, where $N_t^{\pm}$ is the number of events with the truth-level charge specified in the superscript. Charge-misidentification corrections based on the measured rates from ee pairs are applied as event weights to the simulated events.

For ee pairs, the weight for events with incorrectly reconstructed charges is the data-to-simulation ratio m_{ee-d}/m_{ee-s}, where the $\pm$ superscripts for the truth-level charge are suppressed for clarity, and the m_{ee-d} and m_{ee-s} symbols are the misidentification rates observed in the data and simulation, respectively. For $e\nu$ pairs, only $m_{e\nu-s}$ is measured, and it differs from m_{ee-s}. In addition to the alignment of the PES wedge, there is an effect from the differences in the P_T distributions of the electrons (positrons) from γ^*/Z- and W-boson decays.

The corrected misidentification rate for $e\nu$ pairs, $m'_{e\nu-s}$, is given by the product $m_{ee-d}(m_{e\nu-s}/m_{ee-s})$. The leading term is the measured rate from ee pairs, and the following term in parentheses is a relative correction that accounts for the additional effect of electron-P_T differences between W- and γ^*/Z-boson decays. The event-weight correction for charge-misidentified events is $m'_{e\nu-s}/m_{e\nu-s}$, and $(1 - m'_{e\nu-s})/(1 - m_{e\nu-s})$ for events with the correct charge.

To confirm the efficacy of the charge-misidentification corrections to the simulated rate of positrons and electrons for the $W \to e\nu$ process, the following asymmetry $A_{\pm} = (n^+ - n^-)/(n^+ + n^-)$, where $n^{+(-)}$ is the number of positrons (electrons) as a function of η_{det}, is used. All of the charge-independent corrections discussed in this section are applied. Charge-misidentification corrections affect the numerator difference, but leave the denominator sum unchanged. Prior to the application of the charge-misidentification corrections, the $A_{\pm}$ asymmetries of the simulation differed from those of the data for $|\eta_{det}| > 1.5$. Disagreements increased with increasing values of $|\eta_{det}|$ and the amount of disagreement varied with the ϕ-sector locations of the positrons and electrons. The amounts of disagreement are large, significant, and different for positive and negative η_{det} regions within a ϕ-sector. After the application of the charge-misidentification corrections, the differences of the ϕ-sector asymmetries of the simulation relative to the data are significantly decreased.

IX. THE A_ℓ MEASUREMENT

Equation (4) is the basis of the asymmetry measurement. The corrections discussed in Sec. VIII are incorporated into the evaluation of the N^+, N^-, $(\epsilon A)^+$, and $(\epsilon A)^-$ quantities. Using the simulation, the product of the efficiency and acceptance is derived bin-by-bin with the formula $(\epsilon A)^{\pm} = N_r^{\pm}/N_g^{\pm}$, where $N_r^{\pm}$ is the number of reconstructed and selected events in a bin of the reconstructed pseudorapidity, and $N_g^{\pm}$ is the number of accepted events at the event-generation level in the corresponding bin of generated pseudorapidity. In the determination of the
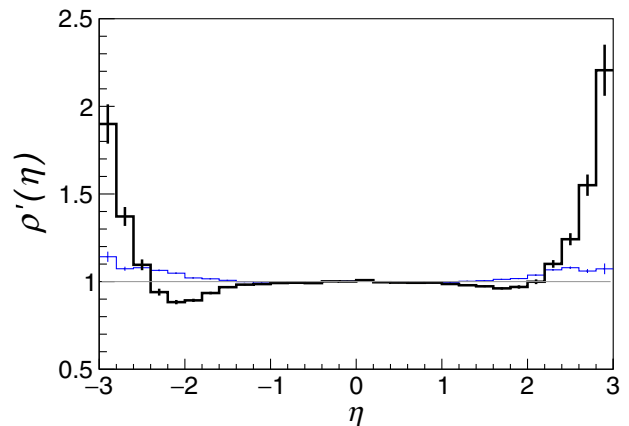

FIG. 15. Dependence of $\rho'(\eta)$ on η. The bold (black) histogram includes the accounting of charge misidentification while the lighter (blue) histogram does not. The uncertainties shown are statistical and are evaluated bin-by-bin. The horizontal (gray) line is a unit-value reference.

generated-level acceptance, the kinematic restrictions on the reconstructed quantities $E_T^e > 25$ GeV, $E_T^\nu > 25$ GeV, and $M_T > 45$ GeV/c^2 are applied to the corresponding generator-level quantities.

Alternatively, the asymmetry can be measured using $(N^+ - \rho N^-)/(N^+ + \rho N^-)$ or $(N^+/\rho - N^-)/(N^+/\rho + N^-)$, where $\rho = (\epsilon A)^+/(\epsilon A)^-$. Figure 15 shows the function $\rho'(\eta)$ defined as $1/\rho$ for the $\eta < 0$ region and ρ for the $\eta \geq 0$ region. The effect of the $\rho'(\eta)$ correction on the measurement can be gauged using $D(\eta) = 1 - 2m(\eta)$, where $D(\eta)$ approximates the ratio of the uncorrected to corrected asymmetry, and $m(\eta)$ is the mean charge-misidentification rate of both charges.

As the A_ℓ distribution is an antisymmetric function of the pseudorapidity, events from the $\eta \geq 0$ and $\eta < 0$ regions provide independent measurements of the asymmetry distribution. They are combined to improve the statistical precision. Prior to the combination, the measurement over the $\eta < 0$ region is transformed via the "CP-folding" operation, $A_\ell(\eta) \to -A_\ell(-\eta)$. The measurement over the $\eta < 0$ region, the measurement over the $\eta \geq 0$ region, and the combined measurement are generically denoted by the symbol $A_\ell(|\eta|)$.

The fully corrected measurements of the $A_\ell(|\eta|)$ from the $\eta \geq 0$ and $\eta < 0$ regions are shown in Fig. 16. The uncertainties shown in Fig. 16 are the diagonal elements of the covariance matrix for the data, which is discussed in the next paragraph. The χ^2 comparison between the $A_\ell(|\eta|)$ measurements of the $\eta \geq 0$ and $\eta < 0$ regions yields a value of 11 over the 15 bins. As the measurements are consistent, they are combined into the CP-folded asymmetry.

Measurement uncertainties require a covariance matrix since the uncertainty of an η bin i and of another bin j are correlated from the measurement uncertainties of the charge-misidentification rates in conjunction with the
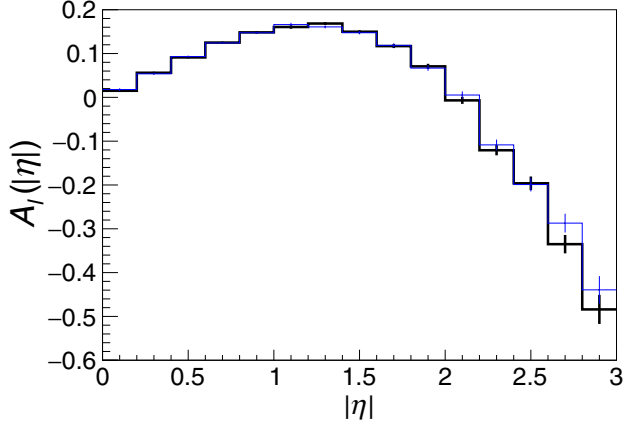
FIG. 16. Observed lepton asymmetry $A_\ell(|\eta|)$ as a function of $|\eta|$. The bold (black) histogram is the measurement in the $\eta \geq 0$ region, and the lighter (blue) histogram is in the $\eta < 0$ region. The measurements include all corrections, and the uncertainties are statistical only, and evaluated bin-by-bin. Bin-centering corrections are not a part of the measurements.

FIG. 17. Eigenvalues λ_n as a function of the eigenvector number n of the covariance matrix for data uncertainties. The eigenvalues, ordered from the largest to the smallest, are numbered from 0 to 14, respectively. The bold (black) histogram shows the eigenvalues, and the lighter (blue) horizontal line corresponds to the smallest value of the diagonal terms of the covariance matrix.

30 cm spread of the $p\bar{p}$-collision vertex along the beam line. The charge-misidentification rate for the tracks traversing a detector region (η_{det}) affects the asymmetry uncertainties of multiple η bins because those tracks are from electrons produced over a wide range of η. The covariance matrix is calculated using the simulation, which provides the distributions for $N_r^\pm$, $N_g^\pm$, and $N_t^\pm$. Recall that $N_r^\pm$ is the number of reconstructed and selected events in a bin of the reconstructed pseudorapidity, $N_g^\pm$ is the number of accepted events at the event-generation level in the corresponding bin of the generated pseudorapidity, and $N_t^\pm$ is the analog of $N_r^\pm$ but with the true charges of the generator level.

In Eq. (4), the $N_r^\pm/(\epsilon A)^\pm$ terms are the corrected event counts $N_c^\pm$ in a data η bin. The $N_r^\pm$ and $(\epsilon A)^\pm$ components contain sums of events from different detector regions. Expressions for the first-order fluctuations of $N_c^\pm$ due to input uncertainties are derived in terms of the fluctuations from its component $N_r^\pm$ and $(\epsilon A)^\pm$ sums. Fluctuation distributions for the $N_r^\pm$ terms are based on the statistical precision of the data, while those for $(\epsilon A)^\pm$ are based on that of the simulation. For both terms, the uncertainties of their $N_r^\pm$ values are estimated using $N_r^\pm = N_t^\pm(1 - m^\pm) + N_t^\mp m^\mp$. Charge-misidentification related uncertainties consist of two components, those from the binomial distribution among the number of events with correctly and incorrectly reconstructed charges, and those from the measured values of $m^\pm$. Uncertainties for the measured values of $m^\pm$ are systematic uncertainties of $(\epsilon A)^\pm$, but they are accounted for here with the statistical uncertainties of $(\epsilon A)^\pm$.

To obtain the final expression for the fluctuations of the asymmetry measurement, the expressions derived for the
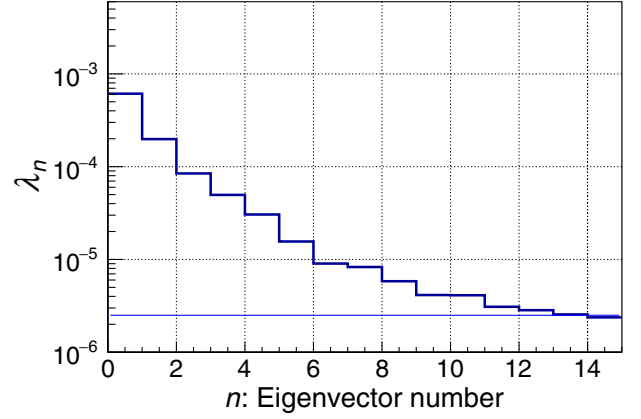
fluctuations of $N_c^\pm$ are incorporated into the asymmetry, Eq. (4). Then, the covariances of fluctuations between the η bins of the measurement are calculated. Two covariance matrices are calculated as there are two asymmetry measurements, the base measurement with 30 bins covering the range $-3 < \eta < 3$ and the combination of the $\eta \geq 0$ and $\eta < 0$ measurements with half the number of bins.

The covariance matrix of uncertainties for the combined measurement, denoted by V, is expanded and inverted to the error matrix using singular-value decomposition methods. As this is a real-valued symmetric 15×15 matrix, its 15 eigenvalues and eigenvectors are the rank-1 matrix components in the decomposition of the covariance matrix and of the error matrix

$$V = \sum_n \lambda_n |v_n\rangle\langle v_n| \text{ and}$$

$$V^{-1} = \sum_n \lambda_n^{-1} |v_n\rangle\langle v_n|, \qquad (5)$$

where λ_n and $|v_n\rangle$ are the eigenvalues and eigenvectors of V, respectively, and $|v_n\rangle\langle v_n|$ represents a vector projection operator in the notation of Dirac bra-kets. In the basis space of the eigenvectors where the error matrix is diagonal, the χ^2 comparison of a calculation to the data is $\sum_n \Delta_n^2/\lambda_n$, where Δ_n is the difference between a calculation and the data along the nth eigenvector, and λ_n represents the squared uncertainty of the difference. Figure 17 shows the eigenvalues. Also shown is the smallest value of the diagonal terms of the covariance matrix. As this value is on par with the smallest eigenvalue, the error matrix does not have any anomalously small eigenvalues that need regulation.

X. SYSTEMATIC UNCERTAINTIES

Systematic uncertainties are evaluated for the electron-energy scales and resolutions, the recoil-system energy scale of the simulation relative to the data, the $|\eta_{\text{det}}|$-dependent scale factors, the backgrounds, and the PDFs. Of these, the PDF uncertainties are the largest.

A. Non-PDF uncertainties

For plug-region events, additional uncertainties are evaluated for the correction of the QCD-background shape at large E_{T} values of the electron, the correction of the simulation efficiency relative to that for data at large $\not{E}_{\text{T}}$ values, and the charge-dependent bias of the track reconstruction. Except for the backgrounds, the uncertainties affect the $(\epsilon A)^{\pm}$ components of the asymmetry measurement. All systematic uncertainties, except those from the PDFs, are small in relation to the statistical uncertainties on the data. The various categories of systematic uncertainties are treated as uncorrelated.

To obtain most of the systematic uncertainties, the corresponding measurement uncertainties are propagated to the asymmetry. The systematic uncertainties of the $|\eta_{\text{det}}|$-dependent scale factors are derived from their statistical uncertainties. One standard-deviation shifts of all $|\eta_{\text{det}}|$ bins are coherently propagated to the asymmetry measurement to obtain upper-limit estimates of the systematic uncertainties. Systematic uncertainties of plug region events due to the QCD-background shape and simulation-efficiency corrections at large $\not{E}_{\text{T}}$ values are taken to be half the difference of the asymmetries observed with and without the correction. For the uncertainty from the plug track-finding bias, the uncertainty of the integrated value of the bias A_{b} is propagated to the asymmetry measurement.

B. PDF uncertainties

Systematic uncertainties due to the PDFs used in the simulation enter through the $(\epsilon A)^{\pm}$ corrections, which depend on the asymmetry. For $(\epsilon A)^{+}$, the explicit expression is

$$\frac{N_{\text{r}}^{+}}{N_{\text{g}}^{+}} = (1 - m^{+})\frac{N_{\text{t}}^{+}}{N_{\text{g}}^{+}} + m^{-}\frac{N_{\text{t}}^{-}}{N_{\text{g}}^{-}}\frac{N_{\text{g}}^{-}}{N_{\text{g}}^{+}},$$

where $N_{\text{g}}^{-}/N_{\text{g}}^{+}$ equals $(1 - A_{\ell})/(1 + A_{\ell})$. The expression for $(\epsilon A)^{-}$ is obtained by interchanging the $+$ and $-$ charge superscripts. The $N_{\text{t}}^{\pm}/N_{\text{g}}^{\pm}$ ratios are the combined efficiencies and acceptances when $m^{\pm} = 0$.

The implementation of PDFs from the NNPDF collaboration that is used in this paper is the ensemble set of 100 equally probable PDFs based on the fit to the input data, along with a default or best-fit PDF. For such probabilistic PDFs, the prediction is the average value of $A_{\ell}(|\eta|)$ calculated over the ensemble, and the dispersion rms about

the average is the PDF uncertainty of the prediction. These uncertainties are correlated across $|\eta|$ bins.

The simulation is used to calculate the covariance matrix of uncertainties due to PDF effects. For the calculation of the corrected number of events $N_{\text{r}}^{\pm}/(\epsilon A)^{\pm}$ in the expression for the asymmetry A_{ℓ}, the data term $N_{\text{r}}^{\pm}$ of the numerator is fixed to its default value from the simulation. The denominator term $(\epsilon A)^{\pm}$ is modified for each ensemble PDF to include its effect on its asymmetry relative to the default. Covariance sums are evaluated using the differences of asymmetries calculated with the modified values of $(\epsilon A)^{\pm}$ relative to the default asymmetries. The eigenvalues and eigenvectors of the covariance matrix are determined with the method used for the covariance matrix of data uncertainties described at the end of Sec. IX. The three largest eigenvalues are comparable to or larger in value than those of the covariance matrix for data uncertainties, but the others are smaller.

C. Total systematic uncertainties

A summary of the minimum and maximum values of the systematic uncertainties from each non-PDF source across the $|\eta|$ bins of the measurement is shown in Table II. Table III shows the data, non-PDF, and PDF uncertainties across the $|\eta|$ bins of the measurement, and Fig. 18 shows the corresponding plot of the data, PDF, and non-PDF uncertainties presented in Table III.

For the total systematic uncertainty, the non-PDF and PDF components are combined. The non-PDF components are negligible, but are added in quadrature with the diagonal elements of the covariance matrix of PDF uncertainties.

XI. RESULTS

The final CDF measurement of the charge asymmetry A_{ℓ} using the electrons from the production and decay of W bosons is presented in Table IV, along with the default NLO

TABLE II. Minimum and maximum values of the systematic uncertainties from each non-PDF source for A_{ℓ} over the $|\eta|$ bins of the measurement. Except for the specific sources of the plug region, the minimum values correspond to $|\eta| \leq 1$ electrons and the maximum values to $|\eta| > 1$. In general, uncertainty values increase with increasing $|\eta|$ values.

Source	Minimum value	Maximum value
Electron-energy scale	3.1×10^{-6}	2.4×10^{-4}
Electron-energy resolution	5.2×10^{-6}	5.9×10^{-5}
Recoil-energy scale	6.5×10^{-6}	3.6×10^{-4}
Efficiency-scale factor	1.2×10^{-6}	6.8×10^{-4}
Backgrounds	7.6×10^{-6}	5.4×10^{-4}
Plug-QCD shape	8.1×10^{-6}	1.5×10^{-4}
Plug high-$\not{E}_{\text{T}}$ efficiency	1.7×10^{-6}	3.2×10^{-5}
Plug track-finding bias	6.0×10^{-7}	6.1×10^{-5}

TABLE III. Data, non-PDF, and PDF uncertainties of each $|\eta|$ bin. The data and PDF uncertainties are taken from the diagonal terms of their respective covariance matrices. The non-PDF entry is the quadrature sum of the non-PDF uncertainties specified in Table II. All uncertainties are bin-by-bin.

$|\eta|$ bin	Data	Non-PDF	PDF
0.0–0.2	2.0×10^{-3}	6.8×10^{-5}	4.0×10^{-6}
0.2–0.4	1.7×10^{-3}	3.2×10^{-5}	2.0×10^{-5}
0.4–0.6	1.6×10^{-3}	1.1×10^{-4}	3.3×10^{-5}
0.6–0.8	1.6×10^{-3}	8.0×10^{-5}	4.9×10^{-5}
0.8–1.0	1.7×10^{-3}	1.1×10^{-4}	6.7×10^{-5}
1.0–1.2	2.8×10^{-3}	1.8×10^{-4}	2.3×10^{-4}
1.2–1.4	2.3×10^{-3}	1.3×10^{-4}	6.2×10^{-4}
1.4–1.6	2.5×10^{-3}	1.5×10^{-4}	1.1×10^{-3}
1.6–1.8	3.3×10^{-3}	1.5×10^{-4}	2.0×10^{-3}
1.8–2.0	4.2×10^{-3}	1.8×10^{-4}	3.0×10^{-3}
2.0–2.2	5.8×10^{-3}	2.1×10^{-4}	4.5×10^{-3}
2.2–2.4	8.4×10^{-3}	5.9×10^{-4}	6.9×10^{-3}
2.4–2.6	1.1×10^{-2}	3.4×10^{-4}	1.0×10^{-2}
2.6–2.8	1.5×10^{-2}	6.3×10^{-4}	1.7×10^{-2}
2.8–3.0	2.3×10^{-2}	8.3×10^{-4}	2.7×10^{-2}

TABLE IV. Electron-asymmetry results compared with predictions of the NLO calculations. The NNPDF 3.0 and NNPDF 3.1 columns respectively show the predictions of the NLO calculations with the NNPDF 3.0 and NNPDF 3.1 PDFs, and the PDF uncertainties shown are evaluated bin-by-bin. The measurement uncertainties shown are from the diagonal elements of the covariance matrix for the measurement.

$|\eta|$ bin	Measurement ($\times 10$)	NNPDF 3.0 ($\times 10$)	NNPDF 3.1 ($\times 10$)
0.0–0.2	0.164 ± 0.020	0.185 ± 0.011	0.184 ± 0.004
0.2–0.4	0.549 ± 0.017	0.549 ± 0.032	0.545 ± 0.011
0.4–0.6	0.921 ± 0.016	0.893 ± 0.049	0.887 ± 0.016
0.6–0.8	1.246 ± 0.016	1.198 ± 0.063	1.190 ± 0.019
0.8–1.0	1.479 ± 0.018	1.442 ± 0.073	1.433 ± 0.023
1.0–1.2	1.634 ± 0.029	1.600 ± 0.081	1.588 ± 0.025
1.2–1.4	1.647 ± 0.024	1.640 ± 0.086	1.621 ± 0.027
1.4–1.6	1.487 ± 0.027	1.525 ± 0.090	1.496 ± 0.030
1.6–1.8	1.178 ± 0.038	1.214 ± 0.094	1.182 ± 0.035
1.8–2.0	0.688 ± 0.052	0.679 ± 0.100	0.656 ± 0.039
2.0–2.2	-0.009 ± 0.073	-0.082 ± 0.109	-0.072 ± 0.046
2.2–2.4	-1.149 ± 0.109	-1.036 ± 0.124	-0.958 ± 0.058
2.4–2.6	-1.976 ± 0.150	-2.134 ± 0.153	-1.930 ± 0.083
2.6–2.8	-3.115 ± 0.225	-3.302 ± 0.210	-2.889 ± 0.137
2.8–3.0	-4.605 ± 0.356	-4.428 ± 0.324	-3.680 ± 0.248

prediction using the NNPDF 3.0 [27]. Uncertainties of the measurement are represented by the sum of the covariance matrices for the statistical uncertainties and the systematic uncertainties. Table IV also includes a calculation using the NNPDF 3.1 PDFs derived with the value of $\alpha_s = 0.118$ at the Z-pole mass [56]. For consistency with the measurement, the predictions using the NNPDF 3.0 and 3.1 PDFs are restricted to the kinematic region of $P_T^e > 25$ GeV/c, $P_T^\nu > 25$ GeV/c, and $M_T > 45$ GeV/c^2.

The input data used in the global fits for the NNPDF 3.0 PDFs do not include any Tevatron measurements of the charge asymmetry in the production of W bosons but do
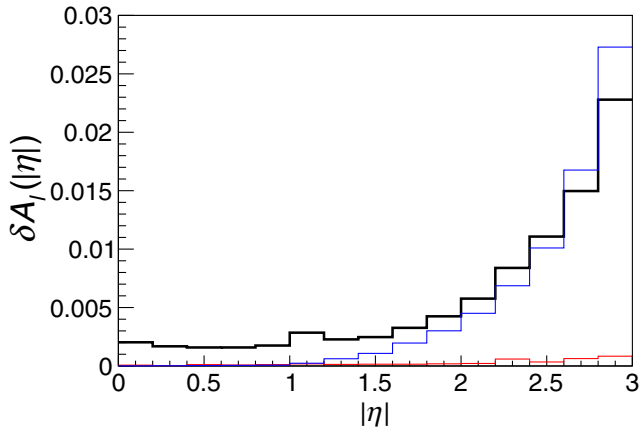

FIG. 18. $\delta A_\ell(|\eta|)$ as a function of $|\eta|$, where δA_ℓ denotes the data, PDF, or non-PDF uncertainty. The bold (black) histogram shows the statistical uncertainty of the data. The lowest (red) histogram is the non-PDF systematic uncertainty. The remaining lighter-shaded (blue) histogram is the uncertainty due to PDFs.

include the lepton-charge asymmetry measurements in the electron and muon channels from CMS using pp collisions at $\sqrt{s} = 7$ TeV [15,16]. The input data for the NNPDF 3.1 PDFs include the final Tevatron measurements of the lepton-charge asymmetry in the electron and muon channels from D0 [7,8]. This inclusion significantly reduces the uncertainty relative to NNPDF 3.0. In addition, the ensemble methodology for NNPDF 3.1 is more robust in that the ensemble represents a better sampling of the probability distribution of the fit to input data.

Figures 19 and 20 show the final results for the charge asymmetry using the electrons at the Tevatron from this measurement and D0 [8]. All uncertainties presented in Table IV and shown in Figs. 19 and 20 are bin-by-bin, and do not reflect their correlations with the uncertainties of neighboring bins. For the data, interbin correlations increase from about 0.03 to about 0.80 as $|\eta|$ increases from 0 to 3.0.

To compare the CDF measurement with predictions, the χ^2 statistic is evaluated over all bins using the error matrix of the measurement. The eigenvalues of the corresponding covariance matrix are shown in Fig. 21. The comparison of the asymmetry measurement with the prediction derived from the NNPDF 3.0 (3.1) ensemble yields the χ^2 value 32.6 (44.9) for the 15 bins of the measurement. Calculation of the corresponding χ^2 value with the bin-by-bin uncertainties of the measurement shown in Table IV instead of the error matrix yields 26.4 (41.2).

The cumulative-χ^2 distribution versus $|\eta|$ as a function of $|\eta|$ is used to assess how the goodness-of-fit varies across
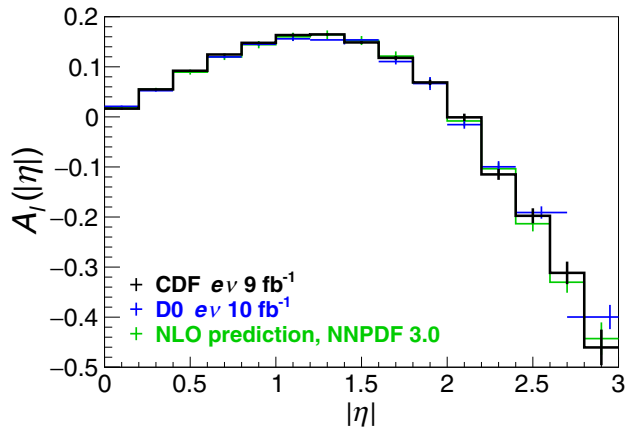
FIG. 19.   CP-folded distributions of $A_\ell(|\eta|)$ as a function of $|\eta|$. The bold (black) histogram is the result of this measurement, and the uncertainties shown are evaluated bin-by-bin and include both statistical and systematic contributions. The (blue) crosses represent the measurement from D0 [8]. For D0, the bin size is also 0.2 $|\eta|$-units wide, except for these regions: 1.2–1.6, 2.4–2.7, and 2.7–3.2. Both the CDF and D0 measurements use all the data from Run II of the Tevatron Collider. The thin (green) histogram is the NLO prediction using the NNPDF 3.0 PDFs.

the $|\eta|$ bins. For the χ^2 evaluated with the error matrix, the χ^2 increment per eigenvector covers several $|\eta|$ bins. Consequently, the increment for each eigenvector is associated with its expectation value of the $|\eta|$-bin centers, $0.1 + 0.2j$, where j is the number of the $|\eta|$ bin, which ranges from 0 to 14. The expectation value is denoted by $|\eta|'$. Figure 22 shows the cumulative-χ^2 distributions versus $|\eta|'$ for the NNPDF 3.0 and 3.1 predictions. These distributions show that the measurement can tighten the constraints to the PDFs over a broad region, $|\eta| > 0.5$.
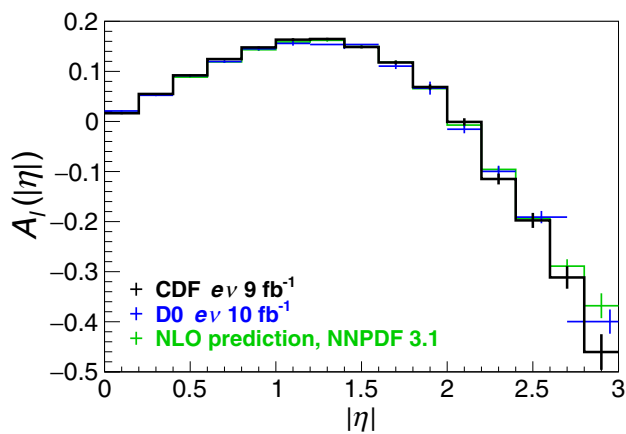

FIG. 20.   Distributions of $A_\ell(|\eta|)$ as a function of $|\eta|$ for the Tevatron measurements previously shown in Fig. 19, along with the NLO prediction with NNPDF 3.1 PDFs. The bold (black) histogram is the result of this measurement and the (blue) crosses the D0 measurement [8]. The thin (green) histogram is the NLO prediction using the NNPDF 3.1 PDFs.
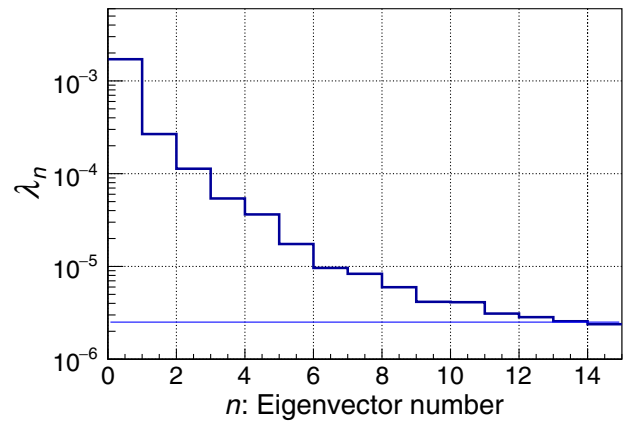

FIG. 21.   Eigenvalues λ_n as a function of the eigenvector number n from the covariance matrix of the asymmetry measurement. The bold (black) histogram shows the eigenvalues, and the lighter (blue) horizontal line corresponds to the smallest value of the diagonal terms of the covariance matrix.

Since each of the ensemble PDFs is equally probable, the distribution of χ^2 values from the comparisons between the measurement and the individual predictions from each of the ensemble PDFs quantifies the consistency between the ensemble and the underlying PDFs of the measurement. Figure 23 shows the χ^2 distributions for the NNPDF 3.0 and NNPDF 3.1 ensemble of PDFs. As the mean and rms of the NNPDF 3.1 ensemble distribution are much smaller than those of NNPDF 3.0, the NNPDF 3.1 ensemble is thus found to be a more robust representation of the Tevatron PDFs and their uncertainties.

The inclusion of this measurement in global PDF fits will improve the precision of the PDFs over the kinematic region for the Tevatron. Numerical tables for the
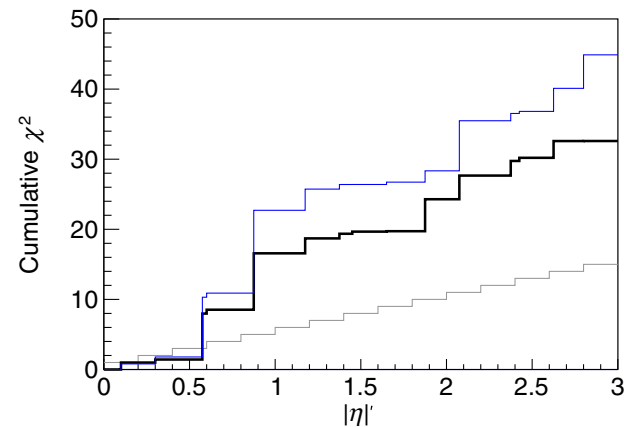

FIG. 22.   Cumulative χ^2 as a function of $|\eta|'$. The bold (black) [light (blue)] histogram is for NNPDF 3.0 [3.1]. The lowermost (gray) histogram is for an ideal 15-bin measurement and a prediction whose underlying physics matches that of the measurement. Differences between the underlying PDFs of the data and that of the calculation result in differences between the ideal and observed χ^2 distributions.
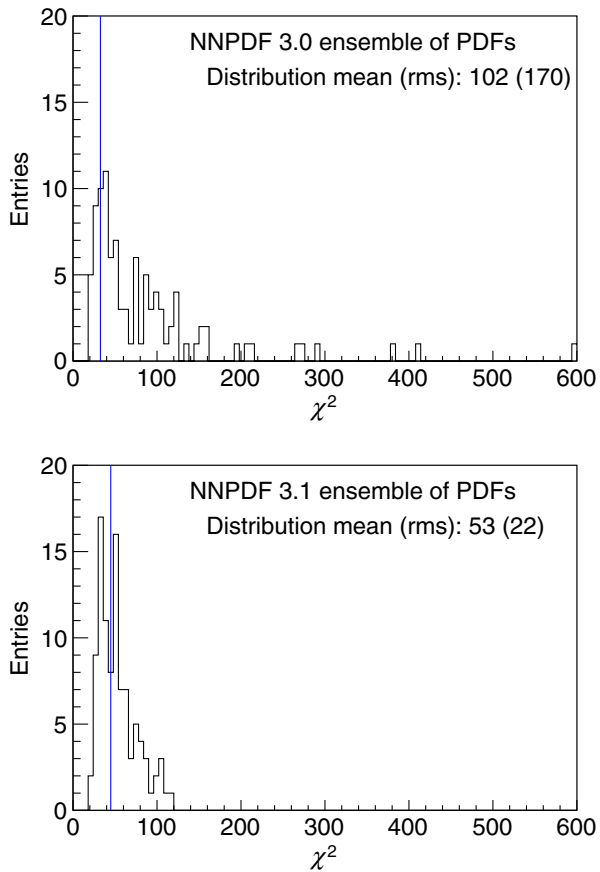
FIG. 23. Distribution of χ^2 values from the comparisons between the measurement and the individual predictions over 15 bins for the NNPDF 3.0 and NNPDF 3.1 ensembles of PDFs. The light (blue) vertical line of each panel show the χ^2 value of the ensemble-averaged prediction for NNPDF 3.0 (32.6) and NNPDF 3.1 (44.9). For NNPDF 3.0, one of the ensemble PDFs gives a χ^2 value of 1548, and is not shown. For NNPDF 3.1, all values are contained within the panel.

measurement and its covariance matrix of uncertainties are provided as supplemental materials to this paper [57]. Also included are numerical tables of the χ^2 values for each PDF of the NNPDF 3.0 and NNPDF 3.1 ensembles.

XII. SUMMARY

The yield asymmetry between positrons and electrons from the decays of $W^{\pm}$ bosons produced in $p\bar{p}$ collisions at the center-of-momentum energy of 1.96 TeV is measured as a function of the electron pseudorapidity using the full Run II data set of CDF, corresponding to 9.1 fb^{-1} of integrated luminosity. Results are in Table IV, and Figs. 19 and 20. The uncertainties in the results are dominated approximately equally by the statistical precision of the data and the effect of PDF uncertainties on the modeling of acceptance and efficiencies.

At the Tevatron collider, the asymmetry is sensitive to the slope of the ratio of d- to u-quark parton-distribution functions of the proton versus the Bjorken-x parameter. Inclusion of this asymmetry measurement in global fits to PDFs will reduce the overall uncertainties of the PDFs within the kinematic region of Tevatron collisions.

APPENDIX: PLUG ELECTRON SELECTION

The background in the plug-electron sample varies significantly with the topology of the reconstructed track in the silicon detector. The purity is adjusted as a function of the quality parameters of the electron candidate, which are the goodness-of-fit between the measured and expected

TABLE V. Selection criteria matrix for plug-region electrons. The index n_l is the number of fiducial layers in the silicon tracker traversed by the particle, and n_h is the number of hits detected in those layers that are associated with the track. In each table-entry pair, the first value is the maximum value for the χ^2_{trk}/n_h quantity, and the second is the maximum value for the $\chi^2_{3\times3}$ quantity.

	$n_h = 3$	$n_h = 4$	$n_h = 5$	$n_h = 6$	$n_h = 7$
$n_l = 7$	2.5/3.0	2.5/4.0	10/10	10/10	10/10
$n_l = 6$	2.5/4.0	2.5/5.0	10/10	10/10	10/10
$n_l = 5$	3.0/3.0	10/3.0	10/3.0	10/3.0	10/3.0
$n_l = 4$	10/3.0	10/3.0	10/3.0	10/3.0	10/3.0
$n_l = 3$	10/3.0	10/3.0	10/3.0	10/3.0	10/3.0

FIG. 24. $\not{E}_T$ distribution for plug-region electrons accepted by the additional selection criteria. The (black) crosses are the data, and the (blue) histogram is the simulation. The online-trigger selection allows the peak at low values of $\not{E}_T$.
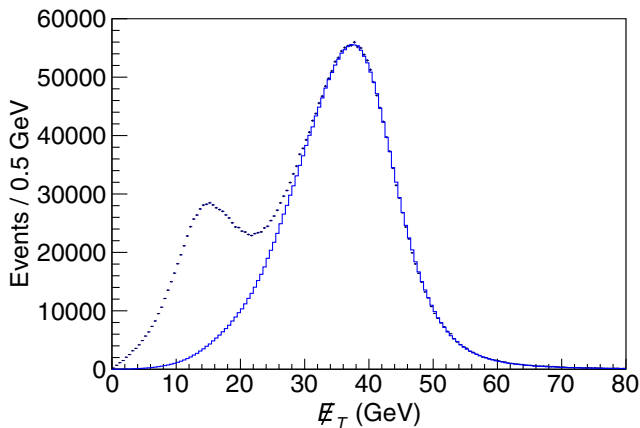

FIG. 25. $\not{E}_T$ distribution for plug-region electrons rejected by the additional selection criteria. The (black) crosses are the data, and the (blue) histogram is the simulation, which contains about 18% of the events without the additional requirements. The online-trigger selection allows the peak at low values of $\not{E}_T$.

transverse-shower shapes $\chi^2_{3\times3}$, and the goodness-of-fit between the track helix and the hits attached to the helix χ^2_{trk}.

Tracks in the plug region are reconstructed with the calorimetry-seeded tracking algorithm ("Phoenix"), which searches for hits in seven layers of the silicon detector. The tracks are characterized by two parameters, (n_l, n_h), where n_l is the number of fiducial layers of the silicon tracker traversed by the particle, and n_h is the number of hits detected in those layers that are associated with the track by the algorithm. Multiple hits per layer can be attached to the track by the algorithm. The number of layers is a prediction based on the track-helix parameters and a simplified model of the silicon-detector geometry. It restricts the electron candidate to a region of $|\eta_{\text{det}}|$.

The maximum allowed χ^2_{trk}/n_h and $\chi^2_{3\times3}$ values are both 10 in the default selection. For electron candidates with lower quality tracks, the maximum χ^2 values are reduced to improve the signal purity. For events with high-E_T electrons, the distributions of these quantities are peaked at values of about 1.0 and decrease exponentially beyond the
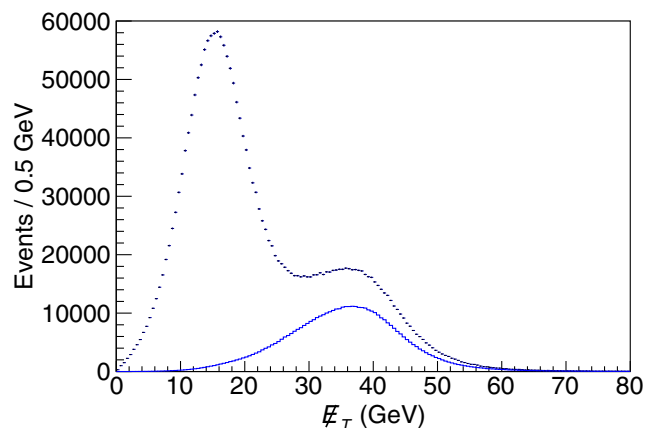
peak. For background events, the distributions are broad and relatively uniform across the χ^2 values in relation to those for the electrons. The events used to adjust the maximum values must pass the asymmetry-measurement criteria of Sec. V C, except for the $\not{E}_T$ criterion. After an adjustment, the $\not{E}_T$ distribution of the event is used to evaluate independently the purity of the electron sample from W-boson decays. The results are shown in Table V.

In addition, the lateral-shower profile measured in the PES detector, which consists of 5 mm wide scintillator strips, is required to be consistent with that of an electron. The profile is measured with the ratio of the shower energy observed in five strips relative to nine strips, $R_{5/9}$. For EM showers, the $R_{5/9}$ distribution is peaked near the value of 0.9. The consistency criterion is $R_{5/9} > 0.75$.

The $\not{E}_T$ distribution after the application of the additional selection criteria is shown in Fig. 24. The $\not{E}_T$ distribution for events passing the default selection criteria but failing the additional criteria is shown in Fig. 25. The simulation is described in Secs. VI and VIII.

[1] S. D. Drell and T.-M. Yan, Phys. Rev. Lett. **25,** 316 (1970); **25,** 902 (1970).

[2] J. D. Bjorken and E. A. Paschos, Phys. Rev. **185,** 1975 (1969).

[3] F. Abe *et al.* (CDF Collaboration), Phys. Rev. Lett. **81,** 5754 (1998).

[4] D. Acosta *et al.* (CDF Collaboration), Phys. Rev. D **71,** 051104(R) (2005).

[5] V. M. Abazov *et al.* (D0 Collaboration), Phys. Rev. D **77,** 011106(R) (2008).

[6] V. M. Abazov *et al.* (D0 Collaboration), Phys. Rev. Lett. **101,** 211801 (2008).

[7] V. M. Abazov *et al.* (D0 Collaboration), Phys. Rev. D **88,** 091102(R) (2013).

[8] V. M. Abazov *et al.* (D0 Collaboration), Phys. Rev. D **91,** 032007 (2015); **91,** 079901 (2015).

[9] T. Aaltonen *et al.* (CDF Collaboration), Phys. Rev. Lett. **102,** 181801 (2009).

[10] V. M. Abazov *et al.* (D0 Collaboration), Phys. Rev. Lett. **112,** 151803 (2014); **114,** 049901 (2015).

[11] A. Bodek, Y. Chung, B.-Y. Han, K. McFarland, and E. Halkiadakis, Phys. Rev. D **77**, 111301(R) (2008).

[12] G. Aad *et al.* (ATLAS Collaboration), Phys. Lett. B **701**, 31 (2011).

[13] M. Aaboud *et al.* (ATLAS Collaboration), Eur. Phys. J. C **77**, 367 (2017).

[14] S. Chatrchyan *et al.* (CMS Collaboration), J. High Energy Phys. 11 (2011) 50.

[15] S. Chatrchyan *et al.* (CMS Collaboration), Phys. Rev. Lett. **109**, 111806 (2012).

[16] S. Chatrchyan *et al.* (CMS Collaboration), Phys. Rev. D **90**, 032004 (2014).

[17] V. Khachatryan *et al.* (CMS Collaboration), Eur. Phys. J. C **76**, 469 (2016).

[18] R. Aaij *et al.* (LHCb Collaboration), J. High Energy Phys. 14 (2014) 079.

[19] R. Aaij *et al.* (LHCb Collaboration), J. High Energy Phys. 16 (2016) 030.

[20] R. Aaij *et al.* (LHCb Collaboration), J. High Energy Phys. 16 (2016) 131.

[21] J. C. Collins and D. E. Soper, Phys. Rev. D **16**, 2219 (1977).

[22] E. Mirkes, Nucl. Phys. **B387**, 3 (1992); E. Mirkes and J. Ohnemus, Phys. Rev. D **50**, 5692 (1994).

[23] S. Frixione, P. Nason, and C. Oleari, J. High Energy Phys. 11 (2007) 070.

[24] S. Alioli, P. Nason, C. Oleari, and E. Re, J. High Energy Phys. 07 (2008) 060.

[25] V. V. Sudakov, Zh. Eksp. Teor. Fiz. **30**, 87 (1956) [Sov. Phys. JETP **3**, 65 (1956)].

[26] T. Sjöstrand, S. Mrenna, and P. Z. Skands, J. High Energy Phys. 05 (2006) 026.

[27] R. D. Ball *et al.* (NNPDF Collaboration), J. High Energy Phys. 04 (2015) 040; Nucl. Phys. **B867**, 244 (2013); R. D. Ball, V. Bertone, F. Cerutti, L. D. Debbio, S. Forte, A. Guffanti, J. I. Latorre, J. Rojo, and M. Ubiali (NNPDF Collaboration), Nucl. Phys. **B855**, 153 (2012); **B849**, 296 (2011); R. D. Ball, L. D. Debbio, S. Forte, A. Guffanti, J. I. Latorre, J. Rojo, and M. Ubiali (NNPDF Collaboration), Nucl. Phys. **B838**, 136 (2010); R. D. Ball, L. D. Debbio, S. Forte, A. Guffanti, J. I. Latorre, A. Piccione, J. Rojo, and M. Ubiali (NNPDF Collaboration), Nucl. Phys. **B809**, 1 (2009); **B816**, 293 (2009); S. Forte, L. Garrido, J. I. Latorre, and A. Piccione, J. High Energy Phys. 05 (2002) 062.

[28] G. A. Ladinsky and C.-P. Yuan, Phys. Rev. D **50**, R4239 (1994); C. Balàzs and C.-P. Yuan, Phys. Rev. D **56**, 5558 (1997); F. Landry, R. Brock, P. M. Nadolsky, and C.-P. Yuan, Phys. Rev. D **67**, 073016 (2003); A. Konychev and P. Nadolsky, Phys. Lett. B **633**, 710 (2006).

[29] P. M. Nadolsky, H.-L. Lai, Q.-H. Cao, J. Huston, J. Pumplin, D. Stump, W.-K. Tung, and C.-P. Yuan (CTEQ Collaboration), Phys. Rev. D **78**, 013004 (2008).

[30] J. C. Collins, D. E. Soper, and G. Sterman, Nucl. Phys. **B250**, 199 (1985); J. C. Collins and D. E. Soper, Nucl. Phys. **B193**, 381 (1981); **B197**, 446 (1982); **B213**, 545(E) (1983).

[31] T. Aaltonen *et al.* (CDF Collaboration), Phys. Rev. D **86**, 052010 (2012).

[32] C. Patrignani *et al.* (Particle Data Group), Chin. Phys. C **40**, 100001 (2016).

[33] N. Cabibbo, Phys. Rev. Lett. **10**, 531 (1963).

[34] M. Kobayashi and T. Maskawa, Prog. Theor. Phys. **49**, 652 (1973).

[35] A. Abulencia *et al.* (CDF Collaboration), J. Phys. G **34**, 2457 (2007).

[36] T. Affolder *et al.*, Nucl. Instrum. Methods Phys. Res., Sect. A **526**, 249 (2004).

[37] T. Aaltonen *et al.*, Nucl. Instrum. Methods Phys. Res., Sect. A **729**, 153 (2013).

[38] L. Balka *et al.*, Nucl. Instrum. Methods Phys. Res., Sect. A **267**, 272 (1988).

[39] S. Bertolucci *et al.*, Nucl. Instrum. Methods Phys. Res., Sect. A **267**, 301 (1988).

[40] M. Albrow *et al.*, Nucl. Instrum. Methods Phys. Res., Sect. A **480**, 524 (2002).

[41] G. Apollinari, K. Goulianos, P. Melese, and M. Lindgren, Nucl. Instrum. Methods Phys. Res., Sect. A **412**, 515 (1998).

[42] P. de Barbaro, IEEE Trans. Nucl. Sci. **42**, 510 (1995).

[43] T. Aaltonen *et al.* (CDF Collaboration), Phys. Rev. D **93**, 112016 (2016); **95**, 119901 (2017).

[44] T. Sjöstrand, P. Edén, L. Lönnblad, G. Miu, S. Mrenna, and E. Norrbin, Comput. Phys. Commun. **135**, 238 (2001).

[45] H. L. Lai, J. Huston, S. Kuhlmann, J. Morfin, F. Olness, J. F. Owens, J. Pumplin, and W. K. Tung (CTEQ Collaboration), Eur. Phys. J. C **12**, 375 (2000).

[46] T. Affolder *et al.* (CDF Collaboration), Phys. Rev. Lett. **84**, 845 (2000).

[47] M. Albrow *et al.* (Tev4LHC QCD Working Group), arXiv:hep-ph/0610012.

[48] E. Barberio and Z. Was, Comput. Phys. Commun. **79**, 291 (1994); E. Barberio, B. van Eijk, and Z. Was, Comput. Phys. Commun. **66**, 115 (1991).

[49] P. Golonka and Z. Was, Eur. Phys. J. C **45**, 97 (2006).

[50] G. Grindhammer, M. Rudowicz, and S. Peters, Nucl. Instrum. Methods Phys. Res., Sect. A **290**, 469 (1990).

[51] A. Bodek, A. van Dyne, J.-Y. Han, W. Sakumoto, and A. Strelnikov, Eur. Phys. J. C **72**, 2194 (2012).

[52] A. Bhatti *et al.*, Nucl. Instrum. Methods Phys. Res., Sect. A **566**, 375 (2006).

[53] J. M. Campbell and R. K. Ellis, Phys. Rev. D **60**, 113006 (1999).

[54] M. Czakon, P. Fiedler, and A. Mitov, Phys. Rev. Lett. **110**, 252004 (2013).

[55] D. Acosta *et al.*, Nucl. Instrum. Methods Phys. Res., Sect. A **494**, 57 (2002).

[56] R. D. Ball *et al.* (NNPDF Collaboration), Eur. Phys. J. C **77**, 663 (2017).

[57] See Supplemental Material at http://link.aps.org/supplemental/10.1103/PhysRevD.104.092002, for the numerical tables of the measurement and the corresponding NNPDF 3.0 and 3.1 calculations; the covariance matrix of the measurement and its corresponding eigenvalues and eigenvectors; and the χ^2 comparison values of the measurement with each PDF of the NNPDF 3.0 and 3.1 ensembles.

T. Aaltonen,[21] S. Amerio,[39a,39b] D. Amidei,[31] A. Anastassov,[15,w] A. Annovi,[17] J. Antos,[12] G. Apollinari,[15] J. A. Appel,[15] T. Arisawa,[51] A. Artikov,[13] J. Asaadi,[47] W. Ashmanskas,[15] B. Auerbach,[2] A. Aurisano,[47] F. Azfar,[38] W. Badgett,[15] T. Bae,[25] A. Barbaro-Galtieri,[26] V. E. Barnes,[43] B. A. Barnett,[23] P. Barria,[41a,41c] P. Bartos,[12] M. Bauce,[39a,39b] F. Bedeschi,[41a] S. Behari,[15] G. Bellettini,[41a,41b] J. Bellinger,[53] D. Benjamin,[14] A. Beretvas,[15,†] A. Bhatti,[45] K. R. Bland,[5] B. Blumenfeld,[23] A. Bocci,[14] A. Bodek,[44] D. Bortoletto,[43] J. Boudreau,[42] A. Boveia,[11] L. Brigliadori,[6a,6b] C. Bromberg,[32] E. Brucken,[21] J. Budagov,[13] H. S. Budd,[44] K. Burkett,[15] G. Busetto,[39a,39b] P. Bussey,[19] P. Butti,[41a,41b] A. Buzatu,[19] A. Calamba,[10] S. Camarda,[4] M. Campanelli,[28] F. Canelli,[11,ee] B. Carls,[22] D. Carlsmith,[53] R. Carosi,[41a] S. Carrillo,[16,†,l] B. Casal,[9,j] M. Casarsa,[48a] A. Castro,[6a,6b] P. Catastini,[20] D. Cauz,[48a,48b,48c] V. Cavaliere,[22] A. Cerri,[26,e] L. Cerrito,[28,r] Y. C. Chen,[1] M. Chertok,[7] G. Chiarelli,[41a] G. Chlachidze,[15] K. Cho,[25] D. Chokheli,[13] A. Clark,[18] C. Clarke,[52] M. E. Convery,[15] J. Conway,[7] M. Corbo,[15,z] M. Cordelli,[17] C. A. Cox,[7] D. J. Cox,[7] M. Cremonesi,[41a] D. Cruz,[47] J. Cuevas,[9,y] R. Culbertson,[15] N. d'Ascenzo,[15,v] M. Datta,[15,hh] P. de Barbaro,[44] L. Demortier,[45] M. Deninno,[6a†] M. D'Errico,[39a,39b] F. Devoto,[21] A. Di Canto,[41a,41b] B. Di Ruzza,[15,p] J. R. Dittmann,[5] S. Donati,[41a,41b] M. D'Onofrio,[27] M. Dorigo,[48a,48d] A. Driutti,[48a,48b,48c] K. Ebina,[51] R. Edgar,[31] A. Elagin,[11] R. Erbacher,[7] S. Errede,[22] B. Esham,[22] S. Farrington,[38] J. P. Fernández Ramos,[29] R. Field,[16] G. Flanagan,[15,t] R. Forrest,[7] M. Franklin,[20] J. C. Freeman,[15] H. Frisch,[11] Y. Funakoshi,[51] C. Galloni,[41a,41b] A. F. Garfinkel,[43] P. Garosi,[41a,41c] H. Gerberich,[22] E. Gerchtein,[15] S. Giagu,[46a] V. Giakoumopoulou,[3] K. Gibson,[42] C. M. Ginsburg,[15] N. Giokaris,[3†] P. Giromini,[17] V. Glagolev,[13] D. Glenzinski,[15] M. Gold,[34] D. Goldin,[47] A. Golossanov,[15] G. Gomez,[9] G. Gomez-Ceballos,[30] M. Goncharov,[30] O. González López,[29] I. Gorelov,[34] A. T. Goshaw,[14] K. Goulianos,[45] E. Gramellini,[6a] C. Grosso-Pilcher,[11] J. Guimaraes da Costa,[20] S. R. Hahn,[15] J. Y. Han,[44] F. Happacher,[17] K. Hara,[49] M. Hare,[50] R. F. Harr,[52] T. Harrington-Taber,[15,m] K. Hatakeyama,[5] C. Hays,[38] J. Heinrich,[40] M. Herndon,[53] A. Hocker,[15] Z. Hong,[47,kk] W. Hopkins,[15,f] S. Hou,[1] R. E. Hughes,[35] U. Husemann,[54] M. Hussein,[32,cc] J. Huston,[32] G. Introzzi,[41a,41e,41f] M. Iori,[46a,46b] A. Isgrò,[41a,41b] A. Ivanov,[7,o] E. James,[15] D. Jang,[10] B. Jayatilaka,[15] E. J. Jeon,[25] S. Jindariani,[15] M. Jones,[43] K. K. Joo,[25] S. Y. Jun,[10] T. R. Junk,[15] M. Kambeitz,[24] T. Kamon,[25,47] P. E. Karchin,[52] A. Kasmi,[5] Y. Kato,[37,n] W. Ketchum,[11,ii] J. Keung,[40] B. Kilminster,[15,ee] D. H. Kim,[25] H. S. Kim,[15,bb] J. E. Kim,[25] M. J. Kim,[17] S. H. Kim,[49] S. B. Kim,[25] Y. J. Kim,[25] Y. K. Kim,[11] N. Kimura,[51] M. Kirby,[15] K. Kondo,[51†] D. J. Kong,[25] J. Konigsberg,[16] A. V. Kotwal,[14] M. Kreps,[24] J. Kroll,[40] M. Kruse,[14] T. Kuhr,[24] M. Kurata,[49] A. T. Laasanen,[43] S. Lammel,[15] M. Lancaster,[28] K. Lannon,[35,x] G. Latino,[41a,41c] H. S. Lee,[25] J. S. Lee,[25] S. Leo,[22] S. Leone,[41a] J. D. Lewis,[15] A. Limosani,[14,s] E. Lipeles,[40] A. Lister,[18,a] Q. Liu,[43] T. Liu,[15] S. Lockwitz,[54] A. Loginov,[54†] D. Lucchesi,[39a,39b] A. Lucà,[17,15] J. Lueck,[24] P. Lujan,[26] P. Lukens,[15] G. Lungu,[45] J. Lys,[26†] R. Lysak,[12,d] R. Madrak,[15] P. Maestro,[41a,41c] S. Malik,[45] G. Manca,[27,b] A. Manousakis-Katsikakis,[3] L. Marchese,[6a,jj] F. Margaroli,[46a] P. Marino,[41a,41d] K. Matera,[22] M. E. Mattson,[52] A. Mazzacane,[15] P. Mazzanti,[6a] R. McNulty,[27,i] A. Mehta,[27] P. Mehtala,[21] C. Mesropian,[45] T. Miao,[15] E. Michielin,[39a,39b] D. Mietlicki,[31] A. Mitra,[1] H. Miyake,[49] S. Moed,[15] N. Moggi,[6a] C. S. Moon,[25] R. Moore,[15,ff,gg] M. J. Morello,[41a,41d] A. Mukherjee,[15] Th. Muller,[24] P. Murat,[15] M. Mussini,[6a,6b] J. Nachtman,[15,m] Y. Nagai,[49] J. Naganoma,[51] I. Nakano,[36] A. Napier,[50] J. Nett,[47] T. Nigmanov,[42] L. Nodulman,[2] S. Y. Noh,[25] O. Norniella,[22] L. Oakes,[38] S. H. Oh,[14] Y. D. Oh,[25] T. Okusawa,[37] R. Orava,[21] L. Ortolan,[4] C. Pagliarone,[48a] E. Palencia,[9,e] P. Palni,[34] V. Papadimitriou,[15] W. Parker,[53] G. Pauletta,[48a,48b,48c] M. Paulini,[10] C. Paus,[30] T. J. Phillips,[14] G. Piacentino,[15,q] E. Pianori,[40] J. Pilot,[7] K. Pitts,[22] C. Plager,[8] L. Pondrom,[53] S. Poprocki,[15,f] K. Potamianos,[26] A. Pranko,[26] F. Prokoshin,[13,aa] F. Ptohos,[17,g] G. Punzi,[41a,41b] I. Redondo Fernández,[29] P. Renton,[38] M. Rescigno,[46a] F. Rimondi,[6a†] L. Ristori,[41a,15] A. Robson,[19] T. Rodriguez,[40] S. Rolli,[50,h] M. Ronzani,[41a,41b] R. Roser,[15] J. L. Rosner,[11] F. Ruffini,[41a,41c] A. Ruiz,[9] J. Russ,[10] V. Rusu,[15] W. K. Sakumoto,[44] Y. Sakurai,[51] L. Santi,[48a,48b,48c] K. Sato,[49] V. Saveliev,[15,v] A. Savoy-Navarro,[15,z] P. Schlabach,[15] E. E. Schmidt,[15] T. Schwarz,[31] L. Scodellaro,[9] F. Scuri,[41a] S. Seidel,[34] Y. Seiya,[37] A. Semenov,[13] F. Sforza,[41a,41b] S. Z. Shalhout,[7] T. Shears,[27] P. F. Shepard,[42] M. Shimojima,[49,u] M. Shochet,[11] I. Shreyber-Tecker,[33] A. Simonenko,[13] K. Sliwa,[50] J. R. Smith,[7] F. D. Snider,[15] H. Song,[42] V. Sorin,[4] R. St. Denis,[19†] M. Stancari,[15] D. Stentz,[15,w] J. Strologas,[34] Y. Sudo,[49] A. Sukhanov,[15] I. Suslov,[13] K. Takemasa,[49] Y. Takeuchi,[49] J. Tang,[11] M. Tecchio,[31] P. K. Teng,[1] J. Thom,[15,f] E. Thomson,[40] V. Thukral,[47] D. Toback,[47] S. Tokar,[12] K. Tollefson,[32] T. Tomura,[49] D. Tonelli,[15,e] S. Torre,[17] D. Torretta,[15] P. Totaro,[39a] M. Trovato,[41a,41d] F. Ukegawa,[49] S. Uozumi,[25] F. Vázquez,[16,l] V. Vecchio,[41a,41b] G. Velev,[15] C. Vellidis,[3] C. Vernieri,[41a,41d] M. Vidal,[43] R. Vilar,[9] J. Vizán,[9,dd] M. Vogel,[34] G. Volpi,[17] P. Wagner,[40] R. Wallny,[15,j] S. M. Wang,[1] D. Waters,[28] W. C. Wester III,[15] D. Whiteson,[40,c] A. B. Wicklund,[2] S. Wilbur,[7] H. H. Williams,[40] J. S. Wilson,[31] P. Wilson,[15] B. L. Winer,[35] P. Wittich,[15,f] S. Wolbers,[15] H. Wolfmeister,[35] T. Wright,[31] X. Wu,[18] Z. Wu,[5] K. Yamamoto,[37] D. Yamato,[37] T. Yang,[15] U. K. Yang,[25] Y. C. Yang,[25] W.-M. Yao,[26] G. P. Yeh,[15] K. Yi,[15,m] J. Yoh,[15] K. Yorita,[51] T. Yoshida,[37,k] G. B. Yu,[25] I. Yu,[25] A. M. Zanetti,[48a] Y. Zeng,[14] C. Zhou,[14] and S. Zucchelli[6a,6b]

(CDF Collaboration)[*]

[1]*Institute of Physics, Academia Sinica, Taipei, Taiwan 11529, Republic of China*

[2]*Argonne National Laboratory, Argonne, Illinois 60439, USA*

[3]*National and Kapodistrian University of Athens, 157 71 Athens, Greece*

[4]*Institut de Fisica d'Altes Energies, ICREA, Universitat Autonoma de Barcelona,
E-08193, Bellaterra (Barcelona), Spain*

[5]*Baylor University, Waco, Texas 76798, USA*

[6a]*Istituto Nazionale di Fisica Nucleare Bologna, I-40127 Bologna, Italy*

[6b]*University of Bologna, I-40127 Bologna, Italy*

[7]*University of California, Davis, Davis, California 95616, USA*

[8]*University of California, Los Angeles, Los Angeles, California 90024, USA*

[9]*Instituto de Fisica de Cantabria, CSIC-University of Cantabria, 39005 Santander, Spain*

[10]*Carnegie Mellon University, Pittsburgh, Pennsylvania 15213, USA*

[11]*Enrico Fermi Institute, University of Chicago, Chicago, Illinois 60637, USA*

[12]*Comenius University, 842 48 Bratislava, Slovakia and Institute of Experimental Physics,
040 01 Kosice, Slovakia*

[13]*Joint Institute for Nuclear Research, RU-141980 Dubna, Russia*

[14]*Duke University, Durham, North Carolina 27708, USA*

[15]*Fermi National Accelerator Laboratory, Batavia, Illinois 60510, USA*

[16]*University of Florida, Gainesville, Florida 32611, USA*

[17]*Laboratori Nazionali di Frascati, Istituto Nazionale di Fisica Nucleare, I-00044 Frascati, Italy*

[18]*University of Geneva, CH-1211 Geneva 4, Switzerland*

[19]*Glasgow University, Glasgow G12 8QQ, United Kingdom*

[20]*Harvard University, Cambridge, Massachusetts 02138, USA*

[21]*Division of High Energy Physics, Department of Physics, University of Helsinki, FIN-00014 Helsinki,
Finland and Helsinki Institute of Physics, FIN-00014 Helsinki, Finland*

[22]*University of Illinois, Urbana, Illinois 61801, USA*

[23]*The Johns Hopkins University, Baltimore, Maryland 21218, USA*

[24]*Institut für Experimentelle Kernphysik, Karlsruhe Institute of Technology, D-76131 Karlsruhe, Germany*

[25]*Center for High Energy Physics: Kyungpook National University, Daegu 702-701, Korea, Seoul
National University, Seoul 151-742, Korea, Sungkyunkwan University, Suwon 440-746, Korea, Korea
Institute of Science and Technology Information, Daejeon 305-806, Korea, Chonnam National University,
Gwangju 500-757, Korea, Chonbuk National University, Jeonju 561-756, Korea
and Ewha Womans University, Seoul 120-750, Korea*

[26]*Ernest Orlando Lawrence Berkeley National Laboratory, Berkeley, California 94720, USA*

[27]*University of Liverpool, Liverpool L69 7ZE, United Kingdom*

[28]*University College London, London WC1E 6BT, United Kingdom*

[29]*Centro de Investigaciones Energeticas Medioambientales y Tecnologicas, E-28040 Madrid, Spain*

[30]*Massachusetts Institute of Technology, Cambridge, Massachusetts 02139, USA*

[31]*University of Michigan, Ann Arbor, Michigan 48109, USA*

[32]*Michigan State University, East Lansing, Michigan 48824, USA*

[33]*Institution for Theoretical and Experimental Physics, ITEP, Moscow 117259, Russia*

[34]*University of New Mexico, Albuquerque, New Mexico 87131, USA*

[35]*The Ohio State University, Columbus, Ohio 43210, USA*

[36]*Okayama University, Okayama 700-8530, Japan*

[37]*Osaka City University, Osaka 558-8585, Japan*

[38]*University of Oxford, Oxford OX1 3RH, United Kingdom*

[39a]*Istituto Nazionale di Fisica Nucleare, Sezione di Padova, I-35131 Padova, Italy*

[39b]*University of Padova, I-35131 Padova, Italy*

[40]*University of Pennsylvania, Philadelphia, Pennsylvania 19104, USA*

[41a]*Istituto Nazionale di Fisica Nucleare Pisa, I-56127 Pisa, Italy*

[41b]*University of Pisa, I-56127 Pisa, Italy*

[41c]*University of Siena, I-56127 Pisa, Italy*

[41d]*Scuola Normale Superiore, I-56127 Pisa, Italy*

[41e]*INFN Pavia, I-27100 Pavia, Italy*

[41f]*University of Pavia, I-27100 Pavia, Italy*

[42]*University of Pittsburgh, Pittsburgh, Pennsylvania 15260, USA*

[43]*Purdue University, West Lafayette, Indiana 47907, USA*

[44]*University of Rochester, Rochester, New York 14627, USA*

[45]*The Rockefeller University, New York, New York 10065, USA*

[46a]*Istituto Nazionale di Fisica Nucleare, Sezione di Roma 1, I-00185 Roma, Italy*
[46b]*Sapienza Università di Roma, I-00185 Roma, Italy*
[47]*Mitchell Institute for Fundamental Physics and Astronomy, Texas A&M University,
College Station, Texas 77843, USA*
[48a]*Istituto Nazionale di Fisica Nucleare Trieste, I-34127 Trieste, Italy*
[48b]*Gruppo Collegato di Udine, I-33100 Udine, Italy*
[48c]*University of Udine, I-33100 Udine, Italy*
[48d]*University of Trieste, I-34127 Trieste, Italy*
[49]*University of Tsukuba, Tsukuba, Ibaraki 305, Japan*
[50]*Tufts University, Medford, Massachusetts 02155, USA*
[51]*Waseda University, Tokyo 169, Japan*
[52]*Wayne State University, Detroit, Michigan 48201, USA*
[53]*University of Wisconsin-Madison, Madison, Wisconsin 53706, USA*
[54]*Yale University, New Haven, Connecticut 06520, USA*

[†]Deceased.
[a]With visitors from University of British Columbia, Vancouver, British Columbia V6T 1Z1, Canada.
[b]With visitors from Istituto Nazionale di Fisica Nucleare, Sezione di Cagliari, 09042 Monserrato (Cagliari), Italy.
[c]With visitors from University of California Irvine, Irvine, California 92697, USA.
[d]With visitors from Institute of Physics, Academy of Sciences of the Czech Republic 182 21, Czech Republic.
[e]With visitors from CERN, CH-1211 Geneva, Switzerland.
[f]With visitors from Cornell University, Ithaca, New York 14853, USA.
[g]With visitors from University of Cyprus, Nicosia CY-1678, Cyprus.
[h]With visitors from Office of Science, U.S. Department of Energy, Washington, D.C. 20585, USA.
[i]With visitors from University College Dublin, Dublin 4, Ireland.
[j]With visitors from ETH, 8092 Zürich, Switzerland.
[k]With visitors from University of Fukui, Fukui City, Fukui Prefecture 910-0017, Japan.
[l]With visitors from Universidad Iberoamericana, Lomas de Santa Fe, México, C.P. 01219, Distrito Federal.
[m]With visitors from University of Iowa, Iowa City, Iowa 52242, USA.
[n]With visitors from Kinki University, Higashi-Osaka City, Japan 577-8502.
[o]With visitors from Kansas State University, Manhattan, Kansas 66506, USA.
[p]With visitors from Brookhaven National Laboratory, Upton, New York 11973, USA.
[q]With visitors from Istituto Nazionale di Fisica Nucleare, Sezione di Lecce, Via Arnesano, I-73100 Lecce, Italy.
[r]With visitors from Queen Mary, University of London, London E1 4NS, United Kingdom.
[s]With visitors from University of Melbourne, Victoria 3010, Australia.
[t]With visitors from Muons, Inc., Batavia, Illinois 60510, USA.
[u]With visitors from Nagasaki Institute of Applied Science, Nagasaki 851-0193, Japan.
[v]With visitors from National Research Nuclear University, Moscow 115409, Russia.
[w]With visitors from Northwestern University, Evanston, Illinois 60208, USA.
[x]With visitors from University of Notre Dame, Notre Dame, Indiana 46556, USA.
[y]With visitors from Universidad de Oviedo, E-33007 Oviedo, Spain.
[z]With visitors from CNRS-IN2P3, Paris, F-75205 France.
[aa]With visitors from Universidad Tecnica Federico Santa Maria, 110v Valparaiso, Chile.
[bb]With visitors from Sejong University, Seoul 143-747, Korea.
[cc]With visitors from The University of Jordan, Amman 11942, Jordan.
[dd]With visitors from Universite catholique de Louvain, 1348 Louvain-La-Neuve, Belgium.
[ee]With visitors from University of Zürich, 8006 Zürich, Switzerland.
[ff]With visitors from Massachusetts General Hospital, Boston, Massachusetts 02114, USA.
[gg]With visitors from Harvard Medical School, Boston, Massachusetts 02114, USA.
[hh]With visitors from Hampton University, Hampton, Virginia 23668, USA.
[ii]With visitors from Los Alamos National Laboratory, Los Alamos, New Mexico 87544, USA.
[jj]With visitors from Università degli Studi di Napoli Federico II, I-80138 Napoli, Italy.
[kk]With visitors from University of Toronto, Toronto, Ontario M5S 1A7, Canada.